This is to certify that the
thesis entitled

DECONVOLUTION OF ATOMIC FORCE MICROSCOPY IMAGE
DATA

presented by

Shiva Arun Kumar

has been accepted towards fulfillment
of the requirements for the

M.S. degree in Electrical Engineering

Lalita Udpa
Major Professor's Signature

January 4, 2007
Date

DECONVOLUTION OF ATOMIC FORCE MICROSCOPY IMAGE DATA

By

Shiva Arun Kumar

A THESIS

Submitted to
Michigan State University
in partial fulfillment of the requirements
for the degree of

MASTER OF SCIENCE

Electrical and Computer Engineering

2007

ABSTRACT

DECONVOLUTION OF ATOMIC FORCE MICROSCOPY IMAGE DATA

By

Shiva Arun Kumar

Atomic Force Microscopy (AFM) is one of a family of Scanning Probe Microscopy (SPM) techniques that has revolutionized the study of structures at atomic scales. AFM has a wide gamut of applications in the fields of semiconductors, biosensors, metallurgy, nanobiology and many others. In AFM a sharp tip is brought within nanometers of a sample and scanned in a raster fashion by means of a piezoelectric scanner while the interaction force is kept constant by a z-feedback mechanism. The tip sample interaction force consists of all possible interatomic forces integrated along the physical structure of the tip over a local region of the sample. The major contributions come from tip and sample atomic nuclei repulsions at distances < 10nm and Van der Waals dipole-dipole attractions at about 100 nm. One of the issues in AFM image analysis is related to artifacts introduced by the interaction between the sample and probe tip. This thesis investigates the application of deconvolution techniques to eliminate the artifacts due to tip shape and help enhance the accuracy of measurements. Specifically, the thesis draws a comparison between two of the popular techniques based on Mathematical Morphology and Legendre Transforms and discusses the equivalence between the two approaches. Results of applying the algorithm on samples of tissue scaffolds validate the potential of the technique in nanobiology.

ACKNOWLEDGEMENTS

Foremost I would like to express my gratitude to my major advisor, Dr. Lalita Udpa. I feel privileged to have had the opportunity of working with her. It was an experience of continuous learning. I am grateful to her and Dr. Satish Udpa for providing me the necessary guidance and support.

I would like to thank my committee members Dr. Virginia Ayres and Dr. Pradeep Ramuhalli for taking the time to serve on my committee and for providing invaluable comments and suggestions to enhance the quality of this dissertation.

Once again I thank each person related to this work directly or indirectly for the successful completion of the thesis.

TABLE OF CONTENTS

List of Figures vii

List of Tables x

Chapter 1 Introduction 1

1.1 Basic Principle and System Setup 2

1.2 Imaging Modes of AFM system. 4

1.2.1 Contact Mode 5

1.2.2 Non-Contact Mode 8

1.2.3 Vibration Mode or Tapping Mode 9

1.3 Applications of Atomic Force Microscopy 11

1.4 Advantages and Limitations of Atomic Force Microscopy. 13

Chapter 2 Image Artifacts in Atomic Force Microscopy 14

2.1 Probe Artifacts 14

2.1.1 Artifacts caused by a blunt tip. 14

2.1.2 Artifacts caused by insufficient probe height. 15

2.1.3 Artifacts caused by chipping of probe surface. 16

2.1.4 Artifacts caused by very sharp sample features. 16

2.2 Scanner Artifacts. 17

2.2.1 Incorrect Probe-Surface Angle 17

2.2.2 X-Y-Z Calibration and linearity 17

2.2.3 Bow/Tilt Artifact 19

2.2.4 Edge Overshoot 19

2.2.5 Scanner Drift. 20

2.2.6 X-Y Angle Measurements. 21

2.2.7 Z Angle Measurements. 21

2.3 Vibrations 22

Chapter 3 Deconvolution of AFM Images 23
3.1 Surface reconstruction and Analysis of AFM images: current status and future trends. 24
3.2 Image Simulation and Surface Reconstruction of AFM images using Legendre Transforms. 25
3.2.1 Basic Principle 26
3.2.2 Image Simulation 26
3.2.3 Surface Reconstruction 29
3.2.4 General relationship between tip, image and sample radii of curvature. 31
3.2.5 Summary 32
3.3 Algorithms for Image Simulation, Surface Reconstruction and Tip Estimation using Mathematical Morphology. 39
3.3.1 Image Model and Image Simulation 40
3.3.2 Surface Recovery and Certainty Maps 44
3.3.3 Blind Tip Estimation 47
3.3.4 Summary & Results 53
3.4 Mathematical equivalence between the Mathematical Morphology and Legendre Transform based Reconstruction Methods. 65
3.4.1 Image Simulation 66
3.4.2 Surface Reconstruction 68

Chapter 4 Deconvolution of AFM data in Nanobiology. 71
4.1 Application of AFM to the study of Polymer Nanofibers. 72
4.1.1 Results of Tip Shape Estimation 74
4.1.2 Results of Deconvolution 77

Chapter 5 Conclusion and Future Work 84

Appendix A: Mathematical Morphology 87

Appendix B: MATLAB Codes 91
Image Simulation: LT Method 91
Surface Reconstruction: LT Method 91
Image Simulation: MM method 93
Surface Reconstruction: MM Method 94
Blind Tip Estimation 94

Kasa's Circle Fit 96

Bibliography 97

LIST OF FIGURES

Figure 1-1 : Basic AFM Setup (7) 4

Figure 1-2 : Contamination of Sample Surface under ambient environmental conditions. 7

Figure 1-3 : Interatomic Force Vs. Distance curve. 8

Figure 2-1 : Broadening of surface features due to blunt probes. 15

Figure 2-2 : Inaccurate depth measurement owing to probe height. 15

Figure 2-3 : Strange artifacts caused by a chipped AFM Probe. 16

Figure 2-4 : Tip artifact caused when imaging a sharp feature with a blunt tip. 16

Figure 2-5 : Artifacts generated by incorrect probe surface angle. 17

Figure 2-6 : Image artifacts caused by non-linear motion of the scanner in the XY direction. 18

Figure 2-7 : Non-Linear motion along Z direction. 18

Figure 2-8 : Bow artifact caused by non-linear piezo motion. 19

Figure 2-9 : Artifacts caused by scanner overshoot along the z-direction. 20

Figure 2-10 : Drift Artifacts caused by temperature fluctuations. 20

Figure 2-11 : XY Angle Measurement 21

Figure 2-12 : Z- Angle Measurement. 21

Figure 3-1 : AFM tip in contact with a steep surface. The true surface height can be found if we know the value of Δx and Δs 28

Figure 3-2 : Determination of true point of contact in Legendre Transform based image simulation. 28

Figure 3-3 : Relationship between the Legendre transform of tip, true surface and image. 31

Figure 3-4 : (a) Sample Surface s(x) (b) Tip Surface $t\Delta x$ (c) $dtd\Delta x$ (d) $dsdx$ 35

Figure 3-5 : Legendre Transform based Image Simulation. 36

Figure 3-6 : Parabolic Tip Surface. 37

Figure 3-7: Image Surface. 38

Figure 3-8: Reconstructed Sample Surface. 38

Figure 3-9: Surface Profile Comparison. 39

Figure 3-10 : Imaging Schematic 41

Figure 3-11: Certainty map for the reconstructed sample surface. 46

Figure 3-12 : Geometry of a reflected probe scanning the underside of an image surface 50

Figure 3-13 : Forcing a particular point on the surface of the reflect tip to touch the image. 53

Figure 3-14 : Tip apex protruding beyond the image surface. 53

Figure 3-15 : Tip shape $t(x, y)$ 55

Figure 3-16 : True Sample Surface $S(x, y)$ 55

Figure 3-17: Simulated Image Surface $I(x, y)$ 56

Figure 3-18 : Profile Comparison. 56

Figure 3-19 : Reconstructed sample surface. 58

Figure 3-20 : Profile comparison with certainty map. 59

Figure 3-21 : Tip estimates at different stages of the blind tip estimation process. 61,62

Figure 3-22 : Comparison between the true tip shape and the estimated tip shape. 63

Figure 3-23 : Surface profile comparison: Really close features on the sample surface seem fused in the reconstructed surface 64

Figure 3-24 Zoomed in version of section 1 in Figure 3-23 64

Figure 3-25 : Surface profile comparison: Thinning effect caused by tip shape. 65

Figure 3-26 : Sample Surface. 69

Figure 3-27 : Surface Profile comparing the reconstructed surface obtained using MM and LT methods with certainty map. 70

Figure 4-1: Polymer nanofibers samples images using AFM.. 74

Figure 4-2 : Tip shape based on manufacturer's specification 75

Figure 4-3 : Blind estimate of tip shape obtained using (a) Sample 1 (b) Sample 2 75,76,77

Figure 4-4 : Reconstructed surface profiles for (a) Sample 1 (b) Sample 2 (c) Sample 3 obtained using manufacturer's tip shape.. 79

Figure 4-5: Kasa Circle Fit 80

Figure 4-6: Histogram of Fiber Width Estimates (Obtained using manufacturer's tip) ... 80

Figure 4-7 : Reconstructed Sample Surface (1) Sample 1 (2) Sample 2 (3) Sample 3.....81

Figure 4-8: Reconstructed Surface Profiles obtained using estimated tip surface....... 81,82

Figure 4-9 : Histogram of fiber width estimates. 83

Figure A1 : (a) Translation of a set S by a vector d (b) Union and Intersection of two sets (1) (c) $A \oplus B$, Dilation of one set by another 88

Figure A2 : Erosion of A by B...89

LIST OF TABLES

Table 1-1 Materials imaged using atomic force microscopy..............................12

Table 4-1 Fiber width estimates in nanometers...82

Chapter 1 Introduction

As the need for high resolution imaging techniques gained importance among Biologists, Organic Chemists, Material Scientists and IC Manufacturers, a new branch of microscopy emerged during the early 1980s with the invention of the Scanning tunneling microscope. This branch of microscopy, popularly known as the Scanning Probe Microscopy (SPM) has spawned a family of microscopy techniques. In SPM a probe raster scans the specimen and records the probe surface interactions as a function of position. The probe-surface interaction of interest depends upon the type of SPM that is being used. Some of the established SPM systems are the Atomic Force Microscope (AFM), Electrostatic Force Microscope (EFM), Force Modulation Microscope (FMM), Magnetic Resonance Force Microscope (MRFM), Near-Field Scanning Optical Microscope (NSOM) and many others (2). Unlike traditional microscopes SPM systems do not use lenses and hence their resolution is only limited by the probe sample interaction volume or the point spread function under question.

Of the several SPM techniques the most popular ones are Scanning Tunneling Microscope (STM) and Atomic Force Microscope. These techniques have a demonstrated resolution of about a fraction of an Angstrom (10^{-10}). The AFM essentially measures surface topography as a contour of constant probe sample interaction force. AFM do not need any current between the sample and tip and hence can be used in imaging of non-conductive samples that are inaccessible to the STM. AFMs are used to image a wide variety of materials such as insulators, organic materials, biological macromolecules, polymers and many others (3) under different environmental conditions and surroundings such as vacuum, liquids under varying temperature conditions.

1.1 Basic Principle and System Setup

The Atomic Force Microscope is a high resolution scanning probe microscope which measures the inter-atomic repulsive forces between atoms and its operation was first demonstrated by Binnig, Quate and Gerber in 1985 (4) (5). The principle of operation of an Atomic Force Microscope is a combination of the principle of the scanning tunneling microscope and the stylus profilometer. During the first demonstration the AFM system used a probe without any damage to the surface of the sample while achieving a lateral resolution of up to 30Å and a vertical resolution of about 1Å while scanning a graphite sample in air. Unlike STM, the AFM can be used to measure the surface topography of both insulators and conductors at atomic resolution.

A basic AFM system (6) as shown in Figure 1.1 consists of the following elements:

1. Tip Sample Interaction.
2. Photodiode sensor to detect the laser light reflected of the sensor.
3. Control Circuitry for the feedback loop.
4. The Piezoelectric scanner or actuator.

The scanning system typically consists of a small cantilever, few micrometers in length, with a sharp probe (tip) at its end which is used to scan the sample surface. The tip is brought in close proximity to the sample surface using the control circuitry and the interatomic repulsive forces between the atoms on the tip and sample surfaces lead to the deflection of the cantilever based on Hooke's Law. The forces that come into play include the mechanical contact force, Van der Waals forces, capillary forces, electrostatic forces, magnetic forces and many others. The prominence of these forces depends on the distance of separation between tip and sample. Usually the deflection of the cantilever is measured using a laser beam that gets deflected from the top of the cantilever surface on to an array of photodiodes. Optical interferometry is another not so commonly used method for detecting the deflection on the cantilever beam. Other less sensitive methods include capacitive sensing or piezoresistive AFM probes where the probe acts as a strain gauge and the strain due to deflection is measured using Wheatstone Bridge.

As suggested earlier the AFM probe is raster scanned across the sample surface but if the height of the tip above the surface is maintained constant during the scanning process then there is a potential risk that the probe would damage the sample surface. In order to avoid this, most often a feedback mechanism is employed to adjust the tip-sample separation that ensures a constant force between tip and sample. The sample to be scanned is usually mounted on a piezoelectric scanner whose motion in the x, y and z directions can be precisely controlled. The scanner can be in the form of a single tube or can be made up of three independent piezoelectric crystals to reduce distortion effects seen in the case of a single piezoelectric tube. The motion of the piezoelectric scanner in the z-direction for every point (x, y) $(s = f(x, y))$ yields the topographic map of the sample surface.

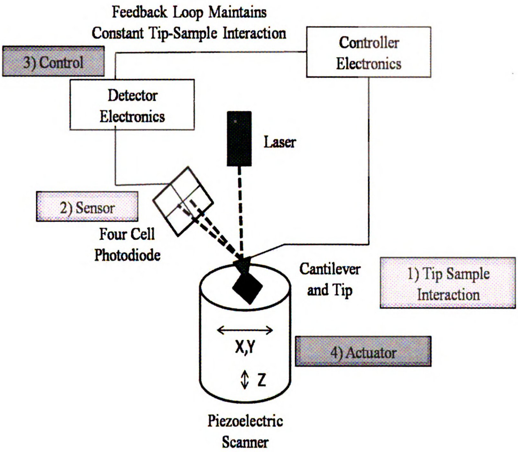

Figure 1-1 : Basic AFM Setup (7)

An AFM system can operate in different modes based on the application on hand. These modes are discussed in detail in the section below.

1.2 Imaging Modes of AFM system.

In its basic configuration we know that the AFM returns the profile of a near field sample surface by raster scanning a probe across it. The deflection of the probe is in accordance with the surface profile and this deflection is digitally captured to yield the topography of the sample. The modes of operation of an AFM can be broadly classified into three basic categories (8):

- Contact Mode
- Non-Contact Mode
- Tapping or Intermittent Contact Mode

A more detailed classification of the modes of operation of an AFM is based on the application on hand and the information that is being collected (9).

1.2.1 Contact Mode

In the contact mode of operation, which is most commonly used, the tip is scanned in close contact with the sample surface. The tip experiences a repulsive force in the order of a few NanoNewtons. In this mode of operation the cantilever is kept in close contact with the sample surface using the piezoelectric positioning element. The deflection of the cantilever is measured and is compared with a desired value of deflection using a DC feedback amplifier. If the measured value is different from the desired value of deflection then the piezoelectric positioning element with sample is moved relative to the cantilever position in order to restore the desired value of deflection. With this feedback system in place the DC potential applied to the piezoelectric positioning element yields the topographic map of the sample surface and is usually displayed as a function of the lateral position on the sample surface. The AFM system in contact mode can operate under various conditions such as Ultra High Vacuum (UHV), air or in liquid medium.

One disadvantage of the contact mode of operation is the excessive forces exerted by the probe on sample surface. This phenomenon is attributed to the problem of surface contamination. Under ambient environmental conditions (room temperature, atmospheric pressure, and ambient air) the sample surface is invariably covered with layer comprising water and miscellaneous hydrocarbons as shown in Figure 1.2. This layer is thick in comparison to the distance between probe surface and the sample. Hence the probe tip is almost always immersed in it and the meniscus formed at this point of contact pulls the cantilever towards the sample surface due to the surface tension experienced by it. Based on the probe to sample separation distance the force between them falls into one of the three regions shown in Figure 1.3.

- The probe experiences no significant influence from the sample surface when the distance between the two is large.
- An attractive zone is created because of the capillary force associated with meniscus formed between the probe surface and the contaminant layer.
- In the repulsive regime the interatomic forces from the sample surface dominate those from the contaminant layer.

Numerous techniques have been suggested for minimizing the tracking forces exerted by the probe on sample surface but there are practical limits to which the magnitude of these forces can be controlled by the user during operation under ambient environmental conditions. One of the methods adopted to neutralize these attractive forces is to operate the AFM system with the probe and part or the entire sample totally immersed in a liquid medium. The advantages of operating the AFM system in a fluid medium include the elimination of capillary forces, reduction of Van der Waal's forces and the ability to study biologically important phenomena at liquid solid interfaces. The disadvantages of imaging in a fluid medium include leaks and sample damage due to the fluid medium. In the case of semiconductors, insulators and other samples, electrostatic charge gets trapped on the surface and is partially dissipated in the fluid medium surrounding it. This charge contributes to additional attractive forces between probe and sample. All of these forces contribute to a minimum nominal force that can be controllably applied by the probe on sample. Under practical situations this nominal value can exceed the normal forces between the probe and sample causing potential damage to the sample, dull the cantilever or even distort the resulting image. Also it is sometimes impractical to immerse semiconductor wafers in a liquid medium. Another method to avoid these frictional forces is the Non-Contact mode of operation of the AFM system.

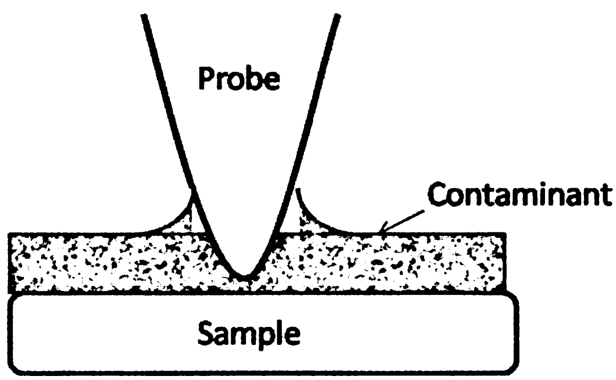

Figure 1-2 : Contamination of Sample Surface under ambient environmental conditions.

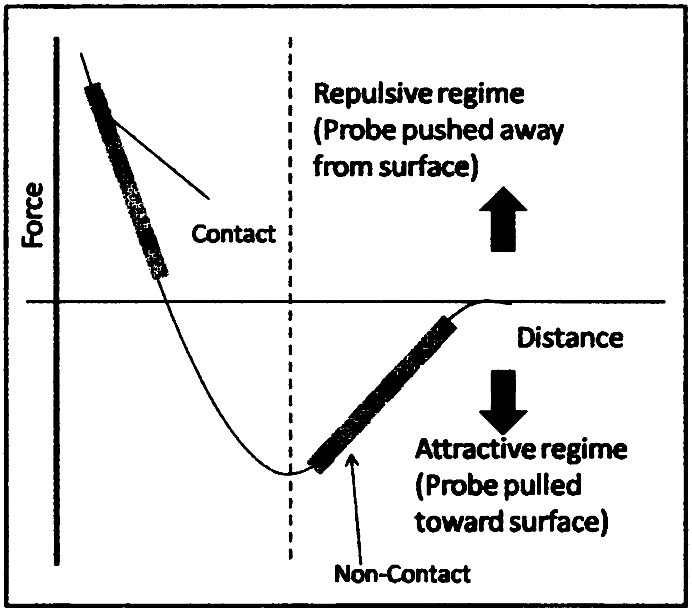

Figure 1-3 : Interatomic Force Vs. Distance curve.

1.2.2 Non-Contact Mode

The first Non-Contact mode AFM (NC-AFM) was developed by Martin et al (10) and paved the way to a new era in the field of imaging. This mode of imaging is used in cases where the probe might change the sample in subtle ways. In NC-AFM imaging, the probe is at a distance of few hundred Angstroms above the sample surface (11) and the cantilever is vibrated at its resonance frequency by a piezoelectric modulator. The amplitude of vibration is maintained at a small value. As the tip approaches the surface, Van der Waals forces between the tip and surface act on the cantilever and cause a change in the amplitude and phase of vibration. These changes are monitored by a feedback system which changes the tip-sample distance accordingly.

It is essential to maintain a considerable tip-sample distance (certain constant value in the order of a few μm) to prevent the tip from contacting the sample surface because if the tip gets stuck to the sample surface it would stop vibrating due to attractive forces exerted by the meniscus between the tip and contaminant layer on the sample surface. This necessitates the use of a high performance z-servo system. In this case it is wise to use a stacked piezo actuator as opposed to a piezo tube. Phase detection is often used with NC-AFM as opposed to amplitude detection because amplitude of vibration is less sensitive to tip sample interaction and the feedback does not perform satisfactorily. One solution to this problem is to increase the tip sample spacing but this would greatly affect the lateral resolution. The quest for a solution is what lead to the tapping mode of operation of an AFM system.

1.2.3 Vibration Mode or Tapping Mode

Tapping mode of operation was a key advancement in AFM technology. This mode of operation yields high resolution images of samples that are very soft, loosely held to their substrate or difficult to image by other AFM techniques. It is panacea to most problems that plague the conventional AFM techniques. Vibration mode of operation overcomes the problems of friction, adhesion and electrostatic forces. The tip on the cantilever is vibrated at its resonant frequency such that it alternately comes in contact with the sample surface thus avoiding the drag forces experienced in the contact mode of operation. The vibration is achieved by means of a piezoelectric crystal. The amplitude of vibration is quite large (on the order of few tens of nanometers) when the tip is not in contact with the sample surface. Now the tip is moved closer to the sample surface till it lightly touches the sample surface as it vibrates. Since tip alternately touches the sample surface and lifts off there is a decrease in the amplitude of vibration due to the loss in energy experienced when the tip comes in contact with the surface. The reduction in the amplitude of oscillation is what is used to identify and measure the surface features of interest.

While operating in tapping mode the feedback system is designed to keep the amplitude of oscillation constant at a desired value. Hence as the tip moves over a bump or a depression the feedback system increases or decreases the tip sample separation to restore the amplitude of oscillation to the desired value. The frequency of oscillation is usually of the order of few hundred kilohertz, which makes the surfaces stiff and hence tip sample adhesive forces are greatly reduced. The tapping mode system has a large operating range and it also helps overcome the problems of shear force since all of the applied force is in the vertical direction. There is a subtle difference between tapping mode of operation in air and in liquid medium. Since the oscillating frequency is damped by liquid medium the entire fluid cell is vibrated to drive the cantilever into oscillation. Cantilevers used in the fluid medium typically have a very low spring constant.

Another very useful extension to the tapping mode of operation is phase imaging. This method of imaging helps provide nanometer scale information of surface structures that are not otherwise obtained using other scanning probe techniques. In addition to surface topography, information regarding composition, adhesive, frictional and viscoelastic properties of sample can be obtained by monitoring the phase of the cantilever oscillation in tapping mode. Some of the applications of phase imaging include identification of surface contaminants in a material and differentiating between regions of high and low adhesion or hardness. The subtle difference between tapping mode and phase imaging is that in the case of phase imaging the phase lag in cantilever oscillation with respect to phase of the signal sent to the cantilever's piezo driver is monitored by the actuator system. This phase information is very sensitive to properties of the material being imaged.

Phase imaging is often used for real time contrast enhancement as it is not affected by large scale height differences and hence helps highlight edges. It provides a clear picture of grain edges which are often obscured by the rough topographic mapping. Phase imaging often complements force imaging methods with superior image detail.

1.3 Applications of Atomic Force Microscopy

The primary application of Atomic Force Microscopy is 3D visualization of surface features whose dimensions are close to the atomic scale. The choice of AFM over other scanning probe techniques stems from the fact that an AFM system can be used to make measurements on wide variety of material types such as conductors, non-conductors, macromolecules and biological specimens. A small set of sample types (12) imaged using an AFM system has been listed under Table 1.1. Other than making surface measurements AFM applications (13) (14) also include:

- Material Evaluation.
    - Surface roughness measurements at the nanometer scale and visualization of surface texture.
    - Surface elasticity measurements.
    - Study of micro-scale friction and adhesion on material surfaces.
    - Study of chemical and physical properties at interfaces of nano-composite polymer materials.

    - Utilize material sensing modes of AFM to differentiate between material types on polymer surface.
    - Quality control of material surfaces.
    - Measurement of magnetic field gradient across material surfaces.
- Non-Destructive Testing.
    - Non-Destructive testing of semiconductor devices.
    - Hot-spot analysis of power electronic devices.
- Nano-Indentation and other surface modifications.

Table 1-1 : Materials imaged using atomic force microscopy.

Inorganic material surfaces	• Silicon wafers. • Ceramics • Digital Storage Media. • Alloys.
Nanostructures	• Nanocrystals • Nanocomposites • Nanotubes • Nanopowders • Nanoceramics
Biological Materials	• Magnetotactic bacteria • DNA • Chromosomes. • Muscle proteins. • Natural resins.

	• Membrane Analysis.

1.4 Advantages and Limitations of Atomic Force Microscopy.

The Atomic Force Microscope has a number of advantages over the electron and the more traditional optical microscopes as listed below:

1. An AFM provides a three-dimensional surface profile unlike the two-dimensional images provided by the electron microscopes.
2. Imaging is done without causing any change or damage to the sample surface.
3. No special treatment or preparation is necessary before scanning a sample.
4. AFM systems can be operated under various environmental conditions such as ambient air, vacuum or even in a liquid medium.
5. It can provide true atomic level resolution.
6. An AFM system is more affordable when compared to a SEM or TEM.

An AFM system suffers from the following limitations:

1. The depth of field in AFM is limited to a few hundred micrometers.
2. The quality of an AFM image is greatly limited by the shape of the probe.
3. AFM has a relatively slow rate of scanning when compared to an SEM which often leads to thermal drift in an image.
4. The quality of AFM images is also affected by hysteresis of the piezoelectric material used.

Chapter 2 Image Artifacts in Atomic Force Microscopy

There are three primary sources of artifacts (15) in any AFM system that introduces distortions in the measured height data.

- Probes
- Scanners
- Vibrations

2.1 Probe Artifacts

As is evident from the principle of operation of an Atomic Force Microscope, the measured topographic data can be modeled as a convolution of the tip shape with surface features on the sample. If the tip or probe used to scan the sample surface is much sharper than the sample features then probe induced artifacts are minimal and the AFM image would be an accurate representation of the true dimensions of surface being imaged. Unfortunately this is not the case in most samples. An optimal size of the probe is chosen based on the surface that is to be scanned.

2.1.1 Artifacts caused by a blunt tip.

If a tip is 'blunt' relative to an object being scanned the measured width of the features appears larger than the true width although the height of the feature is accurately imaged (Figure 2.1).

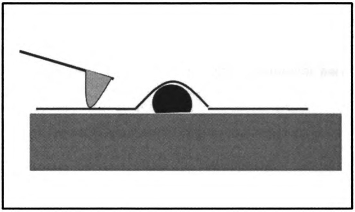

Figure 2-1 : Broadening of surface features due to blunt probes.

2.1.2 Artifacts caused by insufficient probe height.

In certain cases when the sample surface has ridges that are deeper than the probe height the depth of these ridges is inaccurately represented in the AFM image (Figure 2-2). Thus the size of concave features appears smaller than the true size. However, it is possible to measure the opening of the hole accurately. For periodic patterns on a sample surface it is possible to predict the pitch of these patterns accurately.

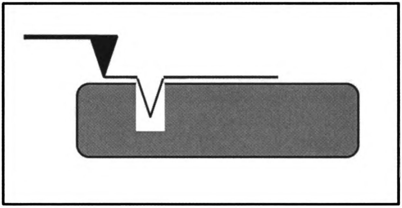

Figure 2-2 : Inaccurate depth measurement owing to probe height.

2.1.3 Artifacts caused by chipping of probe surface.

If the surface of probe breaks or gets chipped other characteristic artifacts would be introduced in the AFM image. This feature becomes prominent particularly when the probe to sample angle is very large (Figure 2-3).

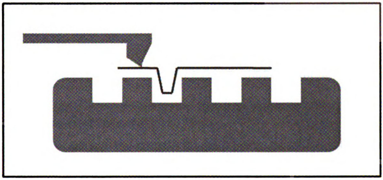

Figure 2-3 : Strange artifacts caused by a chipped AFM Probe.

2.1.4 Artifacts caused by very sharp sample features.

In the case when sample features are much sharper than probe tip, we see periodic patterns on the image surface (Figure 2-4). This is because convolution process causes the tip to be imaged by surface feature rather than the sample being image by the tip. A more detailed discussion about techniques for minimizing the effect of these artifacts is provided in the next chapter.

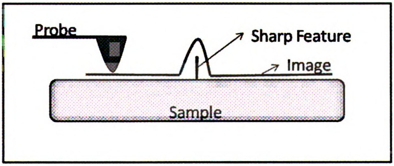

Figure 2-4 : Tip artifact caused when imaging a sharp feature with a blunt tip.

2.2 Scanner Artifacts.

Piezoelectric actuators used in the scanning mechanism for positioning the sample in X, Y and Z coordinate system also introduce errors. In spite of the high resolution achieved using a piezoelectric scanner there are nonlinearities associated with it. For example when a ramp voltage is applied to the scanner its motion exhibits a nonlinear behavior. The scanner also exhibits hysteresis effects. The geometry of scanner and the position of sample relative to the scanner can also lead to AFM image artifacts.

2.2.1 Incorrect Probe-Surface Angle

Another factor that can corrupt the measured AFM data is incorrect probe surface angle (Figure 2-5). In the ideal case the probe is designed to be perpendicular to the surface being scanned. This may not be possible in all AFM systems due to lack of mechanical adjustment screws for the scanner or the probe.

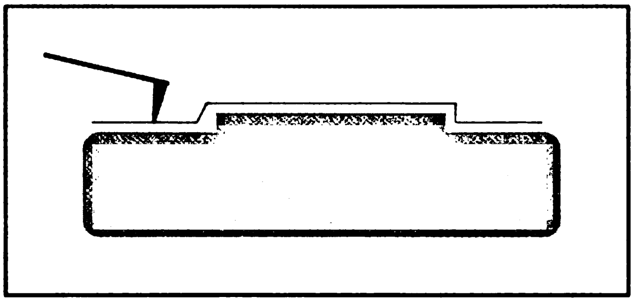

Figure 2-5 : Artifacts generated by incorrect probe surface angle.

2.2.2 X-Y-Z Calibration and linearity

Before using an AFM system it is necessary to calibrate the scanner in X, Y and Z directions and it is also necessary to ensure that the motion of the scanner is linear along these directions. Calibration determines appropriate scaling factors along the scan directions for accurately estimating the measured dimensions. If these correction factors are not included then the AFM image would look compressed on one side and broadened in the other direction.

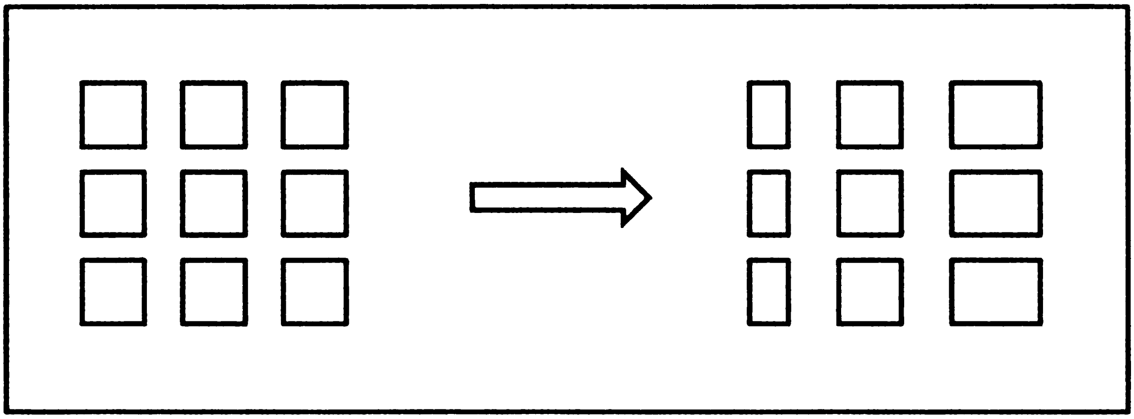

Figure 2-6 : Image artifacts caused by non-linear motion of the scanner in the XY direction. After linearization, if the scanner system has not been calibrated it would lead to incorrect estimation of X, Y values using line profiles. In current systems, calibration sensors are available which would correct the calibration and linearity in real time.

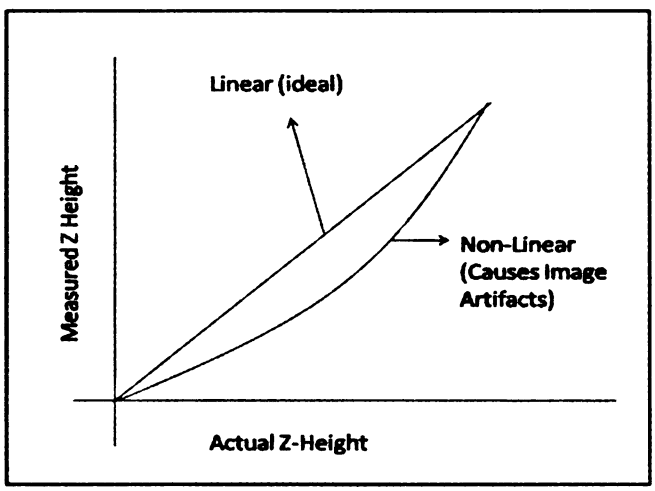

Figure 2-7 : Non-Linear motion along Z direction.

2.2.3 Bow/Tilt Artifact

The piezoelectric scanning system that is used to move the probe along the sample surface very often does not have a straight line motion. The motion path is usually in the shape of a "bow". A further tilt is seen in the image when the probe-surface angle is not 90^{o}. These artifacts can be corrected by applying a baseline compensation algorithm to the image formed by the Atomic Force Microscope.

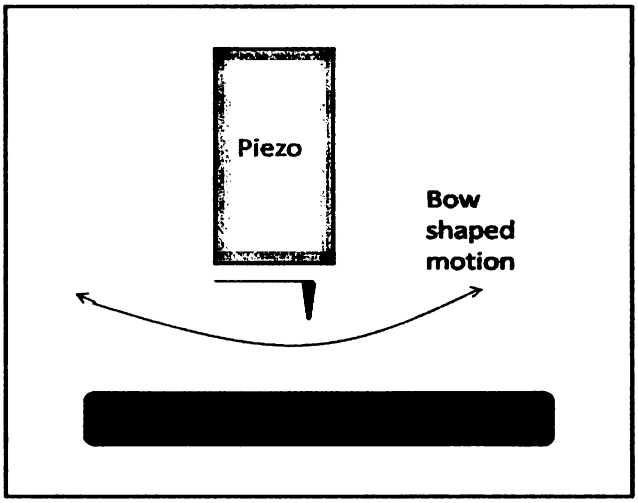

Figure 2-8 : Bow artifact caused by non-linear piezo motion.

2.2.4 Edge Overshoot

This artifact (Figure 2-9) occurs due to the presence of hysteresis in the piezoelectric scanner used to move the probe across the sample surface. This effect is most often encountered while imaging micro-fabricated structures containing sharp change in the height of the sample surface. The edges are enhanced in the image but the height measured along the edges is incorrect.

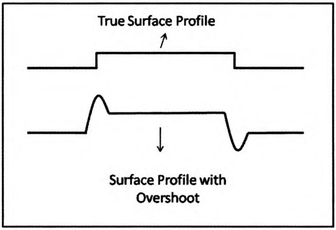

Figure 2-9 : Artifacts caused by scanner overshoot along the z-direction.

2.2.5 Scanner Drift.

A small drift is often seen in AFM data under the influence of external temperature changes. Such distortions are due to drift in the scanner motion owing to temperature fluctuations. They usually occur at the beginning of a scan and cause a linear sample feature to appear curved in the image (Figure 2-10).

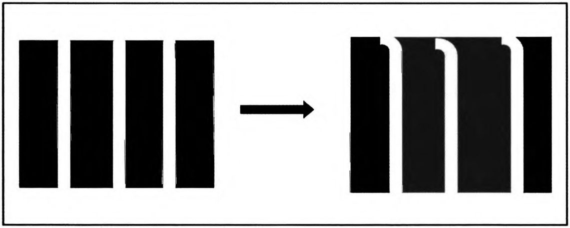

Figure 2-10 : Drift Artifacts caused by temperature fluctuations.

2.2.6 X-Y Angle Measurements.

When the motion of the scanner is not orthogonal in the XY direction there can be 'alignment' errors in the resulting image. They are most evident while imaging repeated patterns on a test sample. Figure 2-11 serves as an example for this type of artifact.

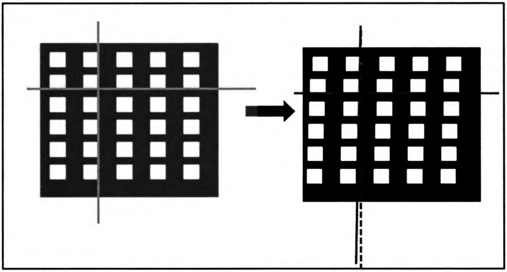

Figure 2-11 : XY Angle Measurement

2.2.7 Z Angle Measurements.

These artifacts are created in the presence of mechanical coupling between the probe scanner motion in the X Y and Z directions. They are most prominent while imaging periodic triangular features on the sample surface (Figure 2-12).

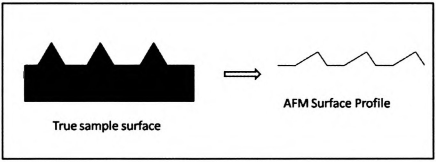

Figure 2-12 : Z- Angle Measurement.

2.3 Vibrations

Another major source of artifacts is due to vibrations present in the AFM system. There are two main sources of vibrations:

- Floor Vibrations: This introduces a periodic noise in the data. Such vibrations can be triggered by external noise sources.
- Acoustic Vibrations.

Chapter 3 Deconvolution of AFM Images

Although Atomic Force Microscopes are widely used to study surface morphologies in materials at nanometer resolution, artifacts in the image introduce errors that mask the true dimensions of surface features. As seen in the previous chapter, there are a number of sources of artifacts in the Atomic Force Microscope data. The most important of these sources is due to the shape of probe surface (16) especially when the sample surface features are much sharper than the probe itself. Since the process of imaging is a convolution process between the probe shape and surface features it is necessary that we design a deconvolution method to extract the true surface topography from any given AFM image. However, implicit in this technique is that we have knowledge of the true shape of the tip. There are several methods suggested in literature for determining the tip shape of which three important ones are i) image the tip using one of the other scanning probe techniques, ii) predict the shape of the tip using the AFM image of a calibration sample known as a tip characterizer (17) iii) use blind tip estimation techniques to get a fair prediction of the probe surface. Each of these methods has its own advantages and limitations which are discussed later in this chapter.

The remainder of this chapter describes existing methods for image simulation, deconvolution or true surface reconstruction and tip shape estimation. Two of the most important methods for surface reconstruction, one based on Mathematical Morphology and the other based on Legendre Transforms are discussed with detailed mathematical derivations. The mathematical equivalence between the two reconstruction methods has also been derived followed by MATLAB results showing the effectiveness of each of these methods.

3.1 Surface reconstruction and Analysis of AFM images: current status and future trends.

Over the years a number of algorithms have been developed to perform surface reconstruction from Atomic Force Microscopy images. These algorithms help reconstruct the tip surface that can then be used to determine the original sample surface by utilizing mathematical models for the imaging process. In this section we discuss some of the popular methods along with their advantages and limitations.

In 1987 a geometric deconvolution algorithm was proposed (18) for reconstructing the sample surface from a given AFM image assuming a spherically shaped probe surface. This assumption limited the wide scale application of this method as the probe shape was not spherical in most practical cases. Stoll (19) in 1991 utilized Wiener Filters to restore the original sample surface from a given AFM image. He designed filters to suppress the effect of significant noise sources in the imaging process and blurring due to finite probe shapes. The algorithm assumed that the point spread function and the noise were independent of the sample surface or "true picture". Hence, the method works well as long as the surface features are shallow or weakly corrugated but fails when sample features are sharp and steep. Subsequently a rigorous mathematical model of the imaging process was developed using the concepts of mathematical morphology (20; 21). A number of engineers and scientists (22) (23) (24) (25) (26) (27) (28) used this model and suggested improvements to achieve a better estimate for the sample surface and also to determine the certainty of the reconstruction process. In 1995 Wang (29) suggested the use of neural networks to correct the integrating effect of finite size tips seen in AFM images. A well trained neural network was used to establish the non-linear mapping between the AFM image and the true sample surface. Some of the drawbacks of the method were i) it assumed the probe surface to have a unique slope at every point which is not true in most practical cases, ii) training of the neural network is in general a tedious task and iii) difficulty in predicting optimal size of the network that would yield accurate results for any given AFM image and probe shape. Other methods include Fourier and Wavelet (30) based analysis and reconstruction of AFM images. These are not based on a mathematical model of the imaging process and the algorithms are application specific. Another drawback in using the wavelet scheme is the choice of scale and type of wavelet to be used for analysis. Lately, the focus has turned towards fusing (31) the information available from images obtained using different SPM techniques. Though each method has its own set of limitations, collectively they can potentially help retrieve all of the information about the original sample surface.

3.2 Image Simulation and Surface Reconstruction of AFM images using Legendre Transforms.

The deconvolution method based on Legendre Transform was first developed by David Keller in 1990. The algorithm designs a non-linear transform to recover the true topographical profile from an AFM image that has been distorted by a non-ideal tip. The author in his paper (32) has shown that this non-linear transform is mathematically related to the Legendre transform of AFM Image and tip surface used to image the sample. The algorithm assumes that one has prior information about the shape of the probe surface used in AFM imaging. Numerical calculations presented in Keller's paper have been derived below followed by a short discussion on the advantages and limitations of this method of reconstruction.

3.2.1 Basic Principle

The basic assumptions made while employing this method are:

- All surfaces under consideration can be represented by a rectangular array of heights sampled at discrete intervals.
- During imaging the tip is in contact with the sample surface at least at one point without compression or penetration of either of the surfaces.
- Image height at any point $\boldsymbol{x}$ is the height of tip apex when the tip is aligned with its apex at $\boldsymbol{x}$ such that the tip just touches the sample surface at some point without violating the previous assumption.

3.2.2 Image Simulation

A schematic of the tip and sample surfaces are shown in Figure 3.1. Let $s(\boldsymbol{x})$ represent the sample surface height at any given point $\boldsymbol{x}$[1]. Let $t(\Delta\boldsymbol{x})$ represent the tip surface where $\Delta\boldsymbol{x}$ is the distance of point $\boldsymbol{x}$ from the tip apex. Let $i(\boldsymbol{x}')$ represent the image surface at any given point $\boldsymbol{x}'$. Therefore the image height can also be represented by the following equation:

$$\boldsymbol{i(x') = t(0,0) + h(x')} \qquad \text{3-1}$$

where $h(\boldsymbol{x}')$ is the height of the tip apex when the tip surface is aligned at $\boldsymbol{x}'$. Keeping in mind the above stated constraints it is evident that the tip surface and the sample surface should be tangential at the true point of contact.

---

[1] Bold faced letters are used to represent two dimensional coordinates. $\boldsymbol{x} = (x, y)$.

$$\frac{ds}{dx}(x) = \frac{dt}{d\Delta x}(\Delta x) \quad \text{3-2}$$

Therefore the first step in image simulation is to eliminate all points that do not satisfy equation 3-2. Ideally, we would like to get a unique solution at the end of the elimination process but based on the surface configuration it is possible that there are multiple locations (x_j for j =1, 2.....n) where condition 3-2 is satisfied. If each of these points yields the same height for the tip apex $i(x')$ then this procedure leads to a solution; otherwise we need to resort to a second step which is an elimination process based on physical grounds that is consistent with assumption 2. In figure 3-2, let x_1, x_2 be two such solutions and the corresponding heights for tip apex be $i_1(x')$ and $i_2(x')$ given ($i_2 < i_1$). Now if i_2 were to be the true height it would mean that the tip surface at location x_1 is below the sample surface which is not possible based on assumption 2. Therefore it is only fair to eliminate location x_2 based on physical grounds. This same process can be repeated for multiple solutions. The image height at any point x' based on Figure 3-1 is

$$i(x') = s(x) - t(\Delta x) \quad \text{3-3}$$

Therefore the second step of elimination can be mathematically expressed as

$$i(x') = max\left(s(x_j) - t(\Delta x_j)\right) \;\; \forall x_j \text{ where j=1,2..} \quad \text{3-4}$$

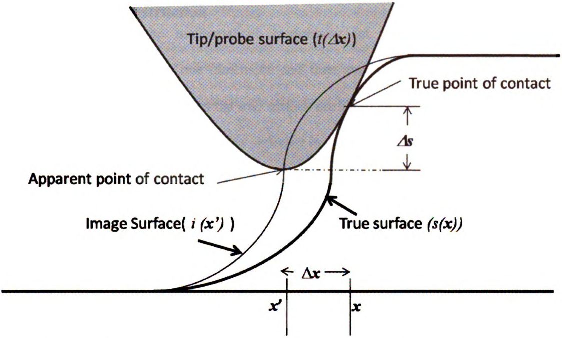

Figure 3-1 : AFM tip in contact with a steep surface. The true surface height can be found if we know the value of Δx and Δs

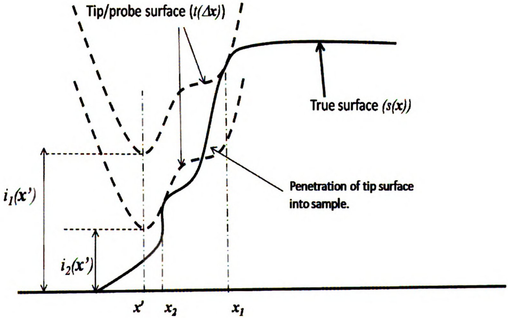

Figure 3-2 : Determination of true point of contact in Legendre Transform based image simulation.

3.2.3 Surface Reconstruction

In order to reduce the mathematical complexity let us first derive the image reconstruction transform in one dimension and then extend to 2D. As is evident from Figure 3-1 it is possible to predict the true surface profile $s(x)$ given the values of Δx and Δs. We will show that the slope of the apparent image surface at x' is equal to the slope of the tip and sample surfaces at x. We can treat Δx and Δs to be functions of x', hence,

$$\Delta x(x') = x - x' \quad \text{.......................................3-5}$$

$$s(x) = i(x') + \Delta s(x') \quad \text{.. ....3-6}$$

Δs can be expressed in terms of the tip surface as follows:

$$\Delta s(x') = t(\Delta x(x'))\ldots \quad \text{..................................3-7}$$

Now differentiating equation 3-5 w.r.t x' we have

$$\frac{dx}{dx'} - \frac{d\Delta x}{(dx')}(x') = 1 \quad \text{.....................................3-8}$$

Differentiating equation 3-6 gives us

$$\frac{di}{dx'}(x') = \frac{ds}{dx}\left(\frac{dx}{dx'} - \frac{d\Delta x}{dx'}\right) \text{..................................3-9}$$

From equations 3-1, 3-8 and 3-9 we have

$$\frac{ds}{dx} = \frac{di}{dx'} = \frac{dt}{d\Delta x} \quad \text{.....................................3-10}$$

Therefore given that we have prior information about the tip and image surfaces we can compute $\Delta x(x')$ which can be used with equation 3-5 to find x' in terms of x. Now $x'(x)$

can be used in equation 3-6 to find the true sample surface $s(x)$. A measure of the degree of distortion is given by differentiating equation 3-10.

$$\frac{d\Delta x}{dx'} = \frac{\left(\frac{d^2 i}{dx'^2}\right)}{\left(\frac{d^2 t}{d\Delta x^2}\right)} \qquad \text{3-11}$$

The relationship between the above mentioned image reconstruction transform and the Legendre transform is very simple. Legendre transform ($L(f(x))$ of a function ($f(x)$) is defined as the intercept made by the tangent to $f(x)$ at x with the y-axis. As evident from Figure 3-3

$$b_{true} = b_{image} + b_{tip} \qquad \text{3-12}$$

$$L(s(x)) = L(i(x')) + L(t(\Delta x)). \qquad \text{3-13}$$

Therefore given the tip and image surface we can compute $L(s(x))$. This implies that the inverse Legendre transform will then yield the true surface topography. One thing to keep in mind is that Legendre transform is a many to one mapping and hence Inverse Legendre transform of $L(s(x))$ may not yield unique height values for all points on the true surface. This leads to the generation of "holes" on the reconstructed sample surface.

Extension of Equation 3-10 to two dimensions is as follows:

$$\frac{\partial t}{\partial \Delta x}(\Delta x) = \frac{\partial s}{\partial x}(x) = \frac{\partial i}{\partial x'}(x') \qquad \text{3-14}$$

Where,

$$\frac{\partial t}{\partial \Delta x} \equiv \left(\frac{\partial t}{\partial \Delta x}, \frac{\partial t}{\partial \Delta y}\right)$$

$$\frac{\partial s}{\partial x} \equiv \left(\frac{\partial s}{\partial x}, \frac{\partial s}{\partial y}\right)$$

$$\frac{\partial i}{\partial x'} \equiv \left(\frac{\partial i}{\partial x'}, \frac{\partial i}{\partial y'}\right)$$

$$L(s(x)) = L(i(x')) + L(t(\Delta x)) \quad \ldots\ldots\ldots\ldots 3\text{-}15$$

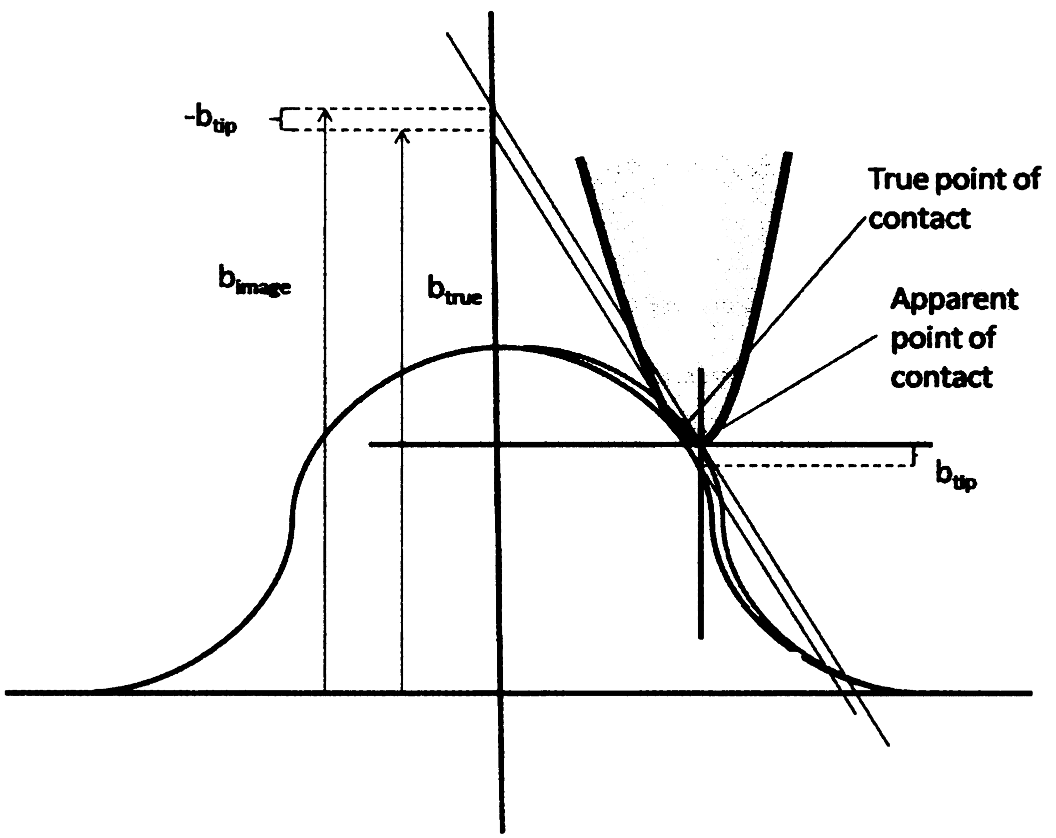

Figure 3-3 : Relationship between the Legendre transform of tip, true surface and image.

3.2.4 General relationship between tip, image and sample radii of curvature.

In one dimension we know that

$$\frac{di}{dx'} = \frac{dt}{d\Delta x}$$

and

$$\frac{ds}{dx} = \frac{dt}{d\Delta x}$$

Differentiating the above equations we have

$$\frac{d^2 i}{dx'^2}(x') = \frac{d^2 t}{d\Delta x^2}(\Delta x) * \frac{d\Delta x}{dx'} \quad \text{...3-16}$$

$$\frac{d^2 s}{dx^2}(x) = \frac{d^2 t}{d\Delta x^2}(\Delta x) * \frac{d\Delta x}{dx} \quad \text{...3-17}$$

Subtracting equation 3-16 from 3-17 and using equation 3-8 we have

$$\left[\frac{d^2 s}{dx^2}(x)\right]^{-1} = \left[\frac{d^2 t}{d\Delta x^2}(\Delta x)\right]^{-1} + \left[\frac{d^2 i}{dx'^2}(x')\right]^{-1} \quad \text{...3-18}$$

3.2.5 Summary

Based on the image model described in the previous section a step by step procedure for image simulation and surface reconstruction using Legendre Transforms is as follows.

Image Simulation:

Let $s(x)$ describe the true sample surface and let $t(\Delta x)$ represent the tip surface, the following steps describe the process of image simulation:

Step 1: Calculate the slopes $\frac{ds}{dx}$ and $\frac{dt}{d\Delta x}$ for every point on the surfaces $s(x)$ and $t(\Delta x)$.

Step 2: For every point x' on the image surface find neighboring points x_j (where j=1, 2,...., n) on the sample surface which satisfy the equation $\frac{ds}{dx}(x_j) = \frac{dt}{d\Delta x}(\Delta x_j)$, where $\Delta x_j = x_j - x$.

Step 3: Now calculate the image surface height at x' using the equation $i(x') = max\left(s(x_j) - t(\Delta x_j)\right) \;\; \forall x_j$ where j=1, 2, 3, ...

Now let us look at the results obtained using this procedure for 1D surface profiles given by $s(x) = \sin(.2x)$ and $t(\Delta x) = .2 * [(\Delta x)^2]/R$ where R is the radius of curvature of the parabolic tip. Now $\frac{ds}{dx} = \cos(.2x)$ and $\frac{dt}{d\Delta x} = [\Delta x/R]$. Let R=16. Figure 3.4 shows the sample and tip surfaces along with its derivates.

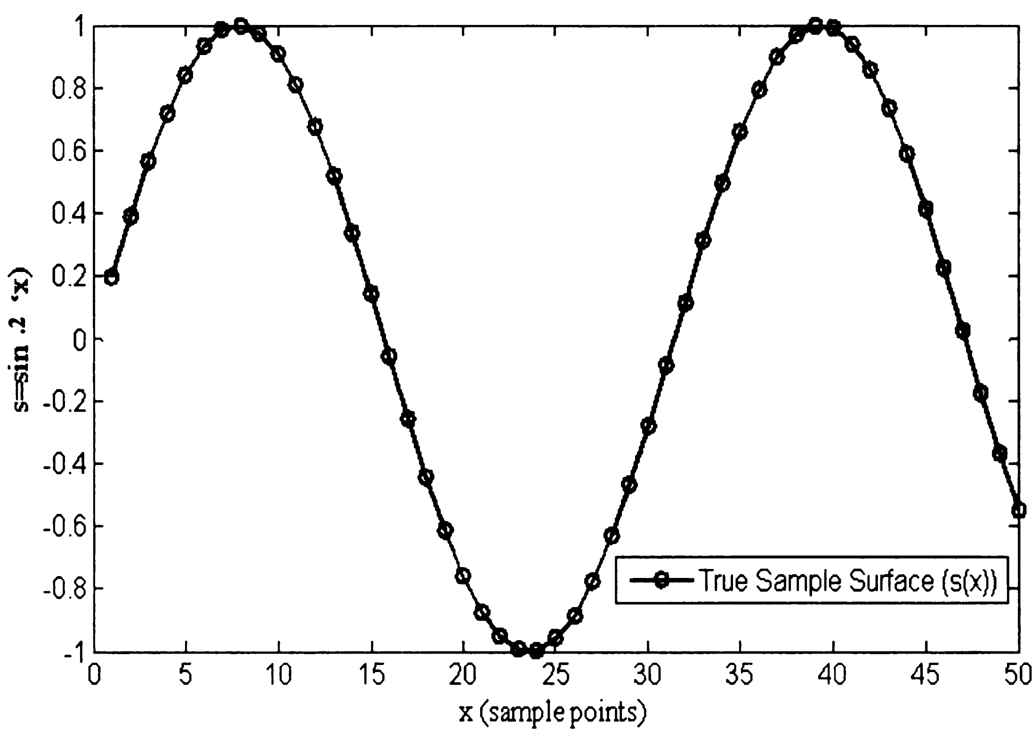

(a)

Figure 3-4: (a) Sample Surface s(x) (b) Tip Surface $t(\Delta x)$ (c) $\frac{dt}{d\Delta x}$ (d) $\frac{ds}{dx}$

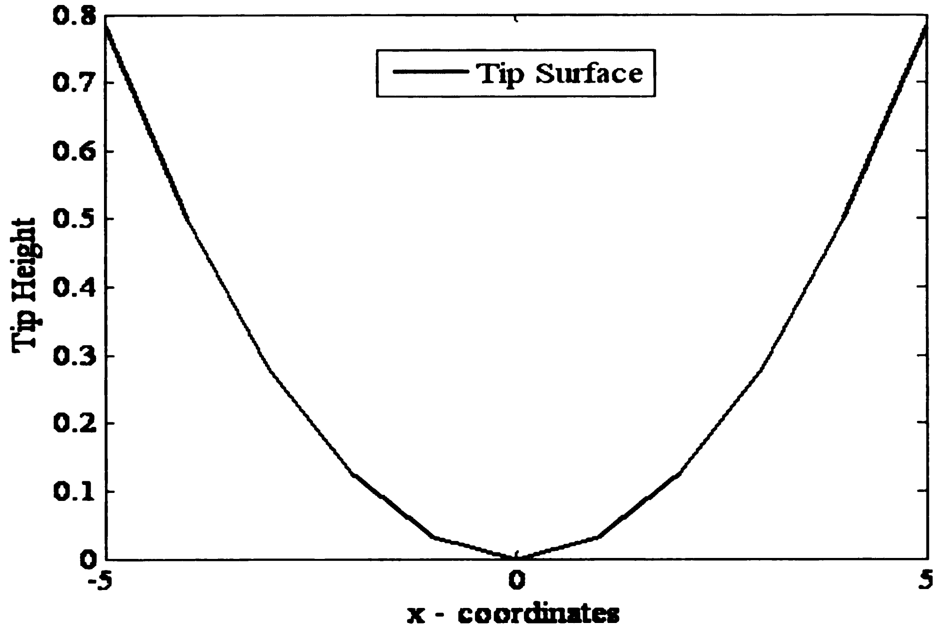

(b)

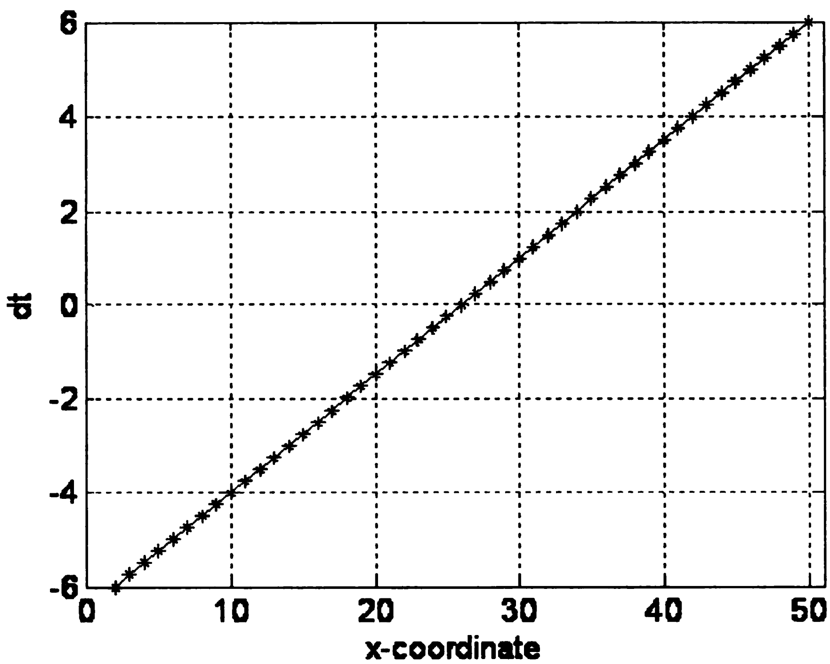

(c)

Figure 3-4: (contd.) (a) Sample Surface s(x) (b) Tip Surface $t(\Delta x)$ (c) $\frac{dt}{d\Delta x}$ (d) $\frac{ds}{dx}$

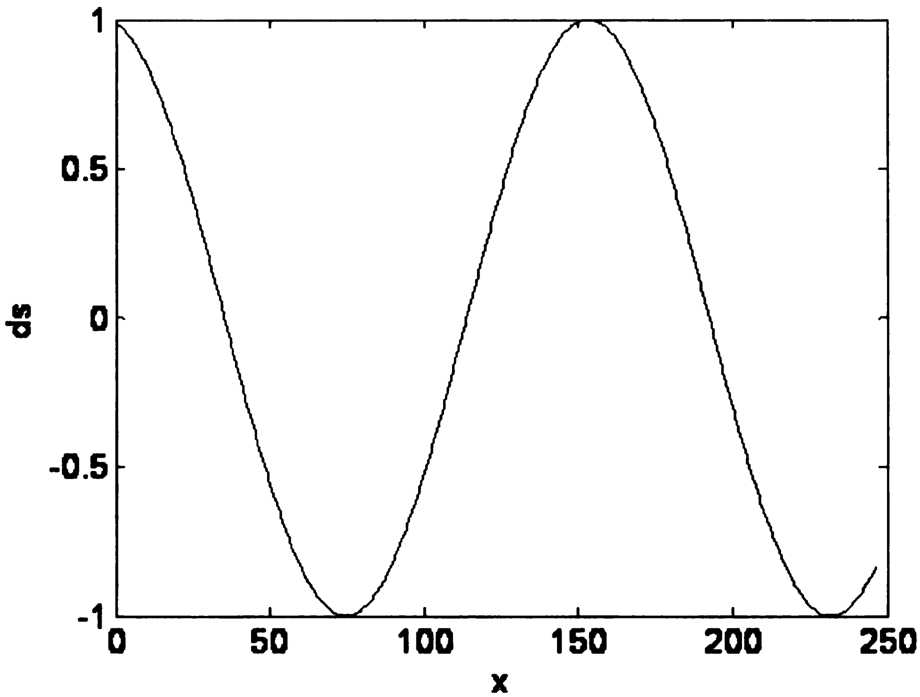

(d)

Figure 3-4 (contd.) : (a) Sample Surface s(x) (b) Tip Surface $t(\Delta x)$ (c) $\frac{dt}{d\Delta x}$ (d) $\frac{ds}{dx}$

The final result after image simulation is as given in Figure 3-5. The necessary MATLAB codes can be found in Appendix B.

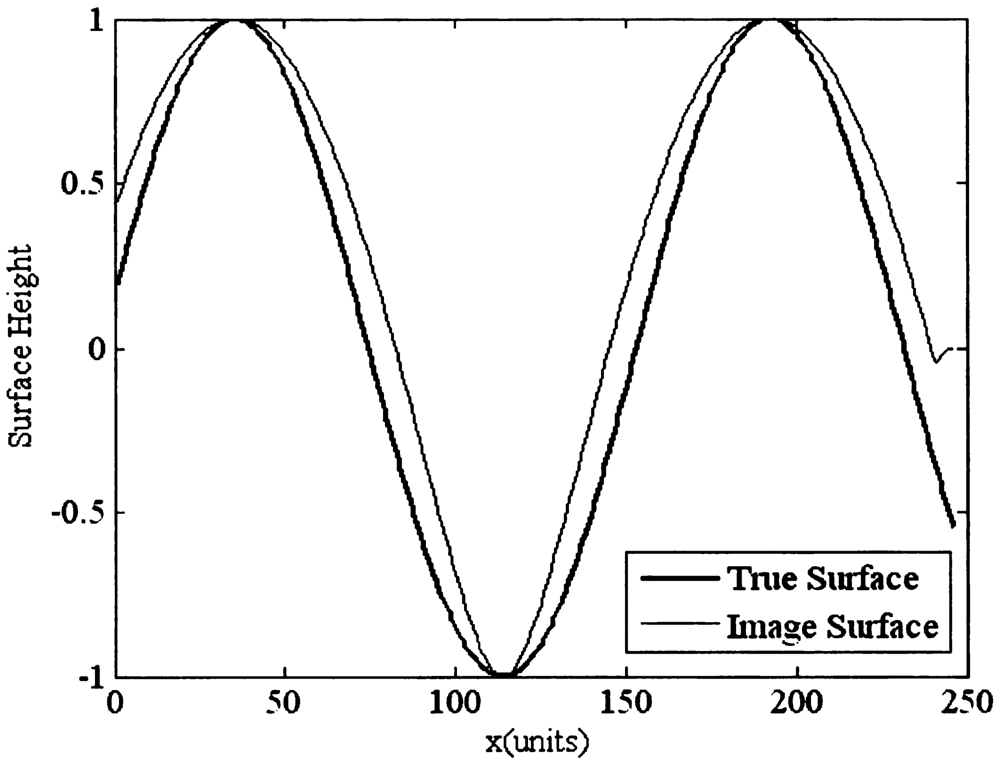

Figure 3-5 : Legendre Transform based Image Simulation.

Surface Reconstruction

Given the image surface $i(x')$ and tip surface $t(\Delta x)$ the procedure for surface reconstruction is as follows:

Step 1: Compute $\frac{dt}{d\Delta x}$ for the given tip surface $t(\Delta x)$.

Step 2: Compute $\frac{di}{dx'}$ for the given image surface $i(x')$.

Step 3: Express Δx in terms of $\frac{di}{dx'}$ using the relation $\frac{\partial t}{\partial \Delta x}(\Delta x) = \frac{\partial i}{\partial x'}(x')$.

Step 4: Compute $\Delta s(x') = t(\Delta x(x')$.

Step 5: Compute $s(x)$ using the relation $s(x) = i(x') + \Delta s(x')$.

Now let us consider a parabolic tip having a radius of curvature equal to 3 as shown in Figure 3-6 ($t(\Delta x)$ =.5*$[\Delta x^2]/3$). Let the image surface $i(x')$ be as shown in Figure 3-7.

Now for the given configuration $\Delta x = R \dfrac{\partial i}{\partial x'}(x')$ and $\Delta s = .5 * R * \left[\dfrac{\partial i}{\partial x'}\right]^2$. Now the reconstructed surface would be as shown in Figure 3-8 and Figure 3-9 compares the profile of the true specimen surface, image surface and reconstructed surface.

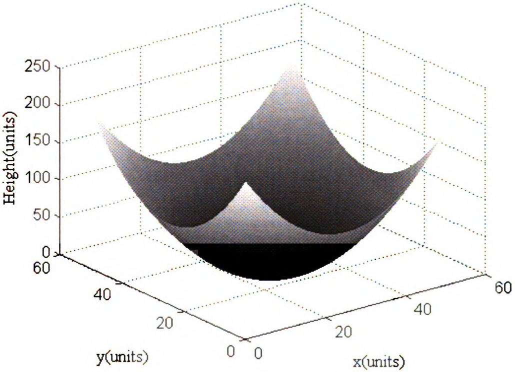

Figure 3-6 : Parabolic Tip Surface.

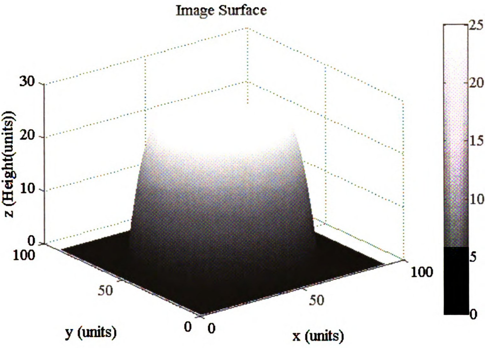

Figure 3-7: Image Surface.

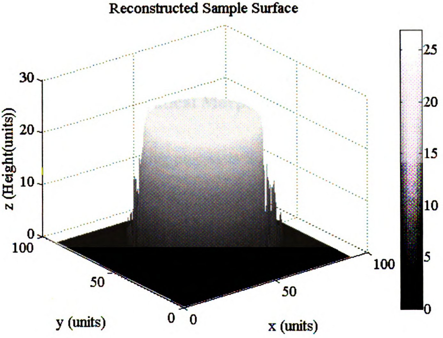

Figure 3-8: Reconstructed Sample Surface.

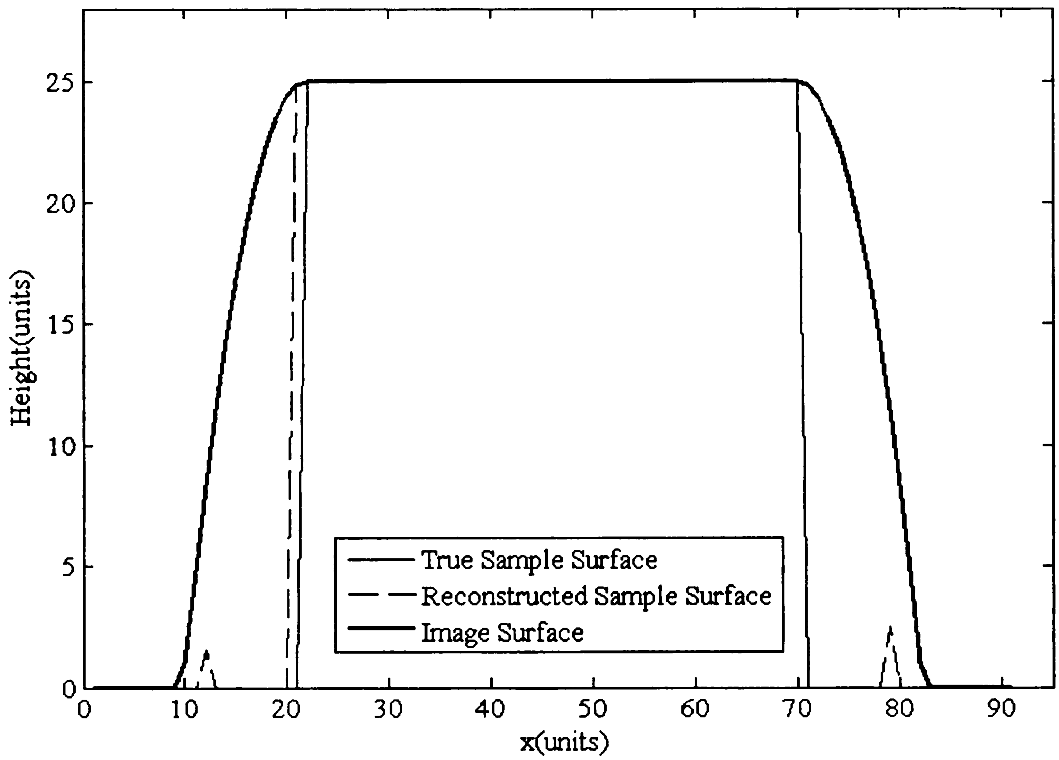

Figure 3-9: Surface Profile Comparison.

3.3 Algorithms for Image Simulation, Surface Reconstruction and Tip Estimation using Mathematical Morphology.

The mathematical model for imaging process in Scanning Probe Microscopy based on Mathematical Morphology was first developed by Gallarda and Jain (20). A rigorous derivation of the governing equation was later presented by Pingali and Jain (21) in 1992. J. S. Villarubia in 1994 provided a method to morphologically estimate the tip shape from an SPM image (27; 1). What follows next in this section is a complete description of the mathematical model adopted for AFM imaging in the contact mode and algorithms for image simulation and surface reconstruction.

3.3.1 Image Model and Image Simulation

There are certain basic assumptions made while designing the model for imaging process in Atomic Force Microscopy:

- $S(x,y)$ is a single valued function, with a finite domain D_S, used to represent the true sample surface.
- $t(x,y)$ is a single valued function with domain D_P used to represent the tip surface.
- As the probe is raster scanned across the sample surface the image output $I(x,y)$ (domain D_I) is assumed to be the height of the tip apex when the tip apex is aligned at point (x,y) and without loss of generality tip apex is assumed to be $t(0,0)$ with a height of zero.

$$t(0,0) = 0 \qquad \text{3-19}$$

- In contact mode of imaging, each image point $I(x, y)$ as stated above is the height of tip apex when the tip is aligned with its apex at (x, y) such that the probe just touches the surface s.
- Non-local effects may be ignored.

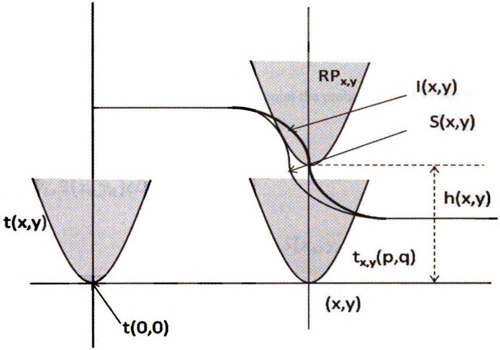

Figure 3-10 : Imaging Schematic

During the imaging process, when the tip is aligned at some point (x, y) on the sample surface it might be raised by height $h(x,y)$ to satisfy all of the assumptions made above. Under these circumstance the surface of the raised probe $(RP_{x,y}(p,q))$ [2] is given by

$$RP_{x,y}(p,q) = t_{x,y}(p,q) + h(x,y) \quad \text{......................3-20}$$

Therefore, $$I(x,y) = RP_{x,y}(x,y) = t_{x,y}(x,y) + h(x,y) \quad \text{...............3-21}$$

$$I(x,y) = t(0,0) + h(x,y) = h(x,y) \quad \text{.....................3-22}$$

[2] *Notation:* We use the notation $f_{a,b}(x,y) = f(x-a, y-b)$ to denote the translation of function f by (a, b).

The assumptions made before enforce certain constraints on the imaging process which can be mathematically expressed as follows:

Constraint 1: In contact mode at every image point the probe surface touches the sample surface at least at one point. Hence,

$\forall (x, y) \epsilon D_I, \exists (x_a, y_a) \epsilon D_S$, such that

$$RP_{x,y}(x_a, y_a) = S(x_a, y_a) \quad \text{3-23}$$

From Figure 3-3 it is clear that

$$I(x, y) = RP_{x,y}(x_a, y_a) - t_{x,y}(x_a, y_a) \quad \text{3-24}$$

$$I(x, y) = S(x_a, y_a) - t_{x,y}(x_a, y_a) \quad \text{3-25}$$

Constraint 2: Corresponding to every image point in contact mode the probe height at every point is always greater than or equal to the sample surface height at the corresponding point. This is to ensure that there is no penetration or compression of surfaces involved.

$\forall (x, y), (x_a, y_a) \epsilon D_S$

$$RP_{x,y}(x_a, y_a) \geq S(x_a, y_a) \quad \text{3-26}$$

Using equations 3-20, 3-22, 3-25 and 3-26 we have

$\forall (x, y), (x_a, y_a) \epsilon D_S$

$$I(x,y) \geq S(x_a, y_a) - t_{x,y}(x_a, y_a) \quad \text{3-27}$$

Or in other words $\forall(x,y), (x_a, y_a) \epsilon D_S$

$$I(x,y) = \max_{(x_a, y_a)} \left(S(x_a, y_a) - t_{x,y}(x_a, y_a) \right) \quad \text{3-28}$$

The above equation completely defines the imaging process and is used for the purpose of image simulation.

It is now shown that the image model derived above is entirely consistent with dilation operation in mathematical morphology. The morphological operation of grayscale dilation " ⊕ " of two functions f and g is defined as follows:

$$f \oplus g = \max_{(x,y) \epsilon D_f} (f(x,y) + g_{x,y}) \quad \text{3-29}$$

From equations 3-28 and 3-29 we have[3]

$$I(x,y) = \max_{(x_a, y_a)} \left(S(x_a, y_a) - t_{x,y}(x_a, y_a) \right)$$

$$I(x,y) = \max_{(x_a, y_a)} (S(x_a, y_a) + rt_{x_a, y_a}(x,y))$$

$$= [S \oplus rt](x,y) \quad \text{3-30}$$

Therefore the imaging process in the contact mode can be represented by the morphological dilation of the true sample surface with the reflected probe surface.

[3]The reflected tip surface is given by $rt(x,y) = -t(-x,-y)$.

3.3.2 Surface Recovery and Certainty Maps

We can now use morphological operations for reconstructing the true sample surface given the distorted image surface ($I(x, y)$) and probe surface ($t(x, y)$). Let $R(x, y)$ represent reconstructed sample surface, based on the constraints specified in section 3.3.1. From equation 3-27 we have $\forall(x, y)(x_a, y_a)\epsilon D_I$

$$S(x, y) \leq I(x_a, y_a) + t_{x_a, y_a}(x, y) \quad \text{......3-31}$$

Or $\forall(x, y)\epsilon D_I$

$$S(x, y) \leq \min_{(x_a, y_a)\epsilon D_I} (I(x_a, y_a) + t_{x_a, y_a}(x, y)) \quad \text{......3-32}$$

$$R(x, y) = \min_{(x_a, y_a)\epsilon D_I} (I(x_a, y_a) + t_{x_a, y_a}(x, y)) \quad \text{......3-33}$$

Now morphological operation of erosion " $\ominus$ " of f by g is given by

$$g \ominus f = \min_{(x, y)\epsilon D_f} (f(x, y) + g(x, y)) \quad \text{......3-34}$$

From equations 3-33 and 3-34 we have

$$R(x, y) = [t \ominus I](x, y) \quad \text{......3-35}$$

Now that we have a reconstructed sample surface it is useful to ascertain where the reconstruction process actually yielded the true sample surface and where it did not. In order to do this we need to go back to the constraints imposed by the imaging process.

We know that $\forall(x, y)\epsilon D_I, \exists(x_a, y_a)\epsilon D_S$

$$S(x_a, y_a) = I(x, y) + t_{x,y}(x_a, y_a) \text{ ....3-36}$$

From equations 3-32 and 3-36 we have $\forall(x, y)\epsilon D_I, \exists(x_a, y_a)\epsilon D_S$ such that

$$S(x_a, y_a) \leq \min_{(x,y)}(I(x, y) + t_{x,y}(x_a, y_a)) \text{ ....3-37}$$

From equations 3-33 and 3-37 we have $\forall(x, y)\epsilon D_I, \exists(x_a, y_a)\epsilon D_S$ such that

$$S(x_a, y_a) = R(x_a, y_a) \text{..............................3-38}$$

Combining Equation 3-38 with 3-36 we have $\forall(x, y)\epsilon D_I, \exists(x_a, y_a)\epsilon D_S$ such that

$$I(x, y) = R(x_a, y_a) - t_{x,y}(x_a, y_a) \text{..............................3-39}$$

And

$$S(x_a, y_a) = R(x_a, y_a) \text{..............................3-40}$$

Now for some point $(x_1, y_1)\epsilon D_I$ if we have only one point $(x_a, y_a)\epsilon D_S$, which satisfies equation 3-39, then we know $S(x_a, y_a) = R(x_a, y_a)$ for the point $(x_a, y_a)\epsilon D_S$.

The above statement can be restated as the following necessary condition for equality of recovered and original surfaces:

$\forall(x, y)\epsilon D_R$, $R(x, y) = S(x, y)$ if $\exists(x_1, y_1)\epsilon D_I$ such that

$R(x, y) = I(x_1, y_1) + t_{x_1,y_1}(x, y)$ and $\forall(x_2, y_2)\epsilon D_R$ and $(x_2, y_2) \neq (x, y)$

$R(x_2, y_2) \neq I(x_1, y_1) + t_{x_1,y_1}(x_2, y_2)$.

In Figure 3-11 all points between x_1 and x_2 satisfy equation 3-39 to yield the same image height at x_1. Hence the certainty of reconstruction at these points is zero. For all other points on the image surface there is a unique contact point on the reconstructed specimen surface where the certainty of reconstruction is one. Certainty of 0 does not necessarily mean that the reconstruction is incorrect; it implies that it is not possible to obtain the correct reconstruction at this point. There is a possibility that in Figure 3-11 the true sample surface between x_1 and x_2 is same as the reconstructed surface between these points. Therefore the above mentioned criterion is not sufficient to conclusively state whether the prediction is incorrect.

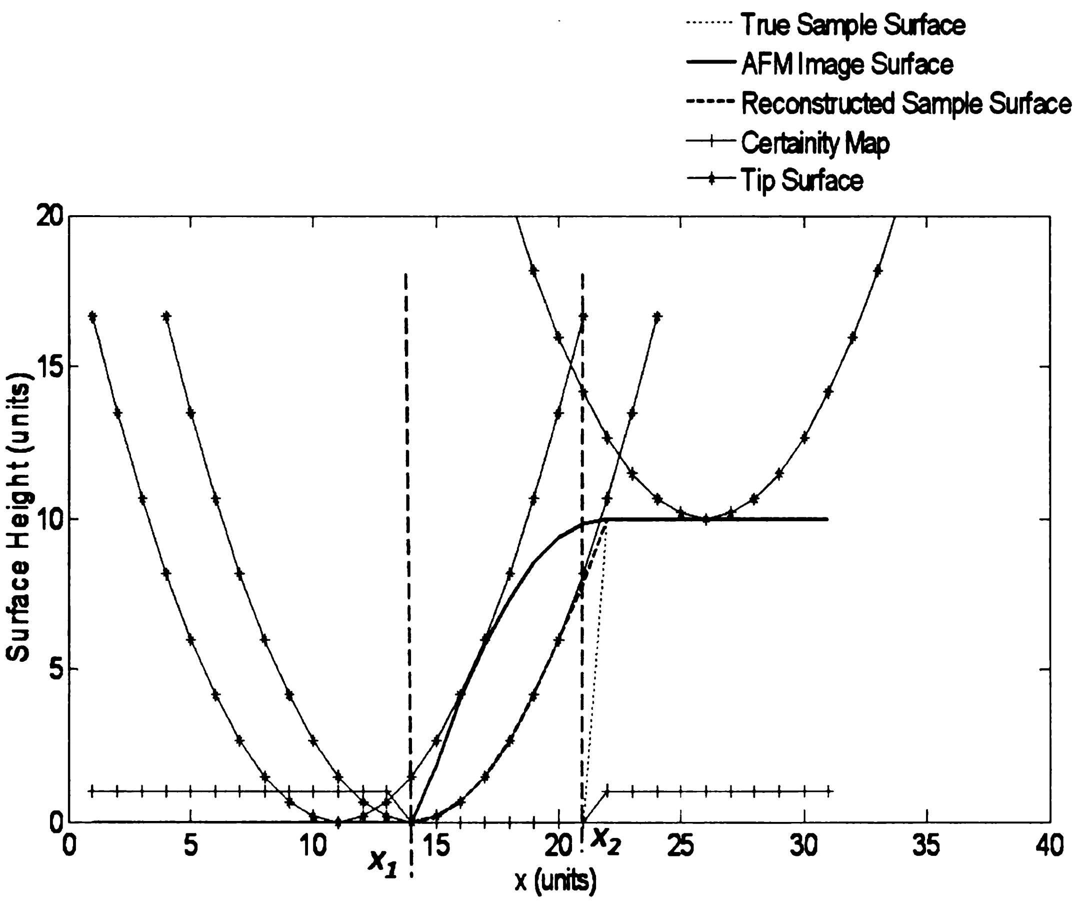

Figure 3-11: Certainty map for the reconstructed sample surface.

3.3.3 Blind Tip Estimation

In the reconstruction algorithms presented above it is necessary to have a 3D model for the tip geometry in order to reconstruct the original sample surface. Most often the information available about the probe geometry is incorrect because probes may abrade or suffer damage during the process of imaging. Therefore it is necessary to re-measure the probe geometry at the end of the scanning process using other imaging techniques like electron microscopy. However, this does not always solve the problem since these imaging techniques are also not exact in that they suffer from artifacts. Given the above situation it is necessary to develop an algorithm for blind estimation of tip geometry given an image of the sample surface. Villarrubia (1) presents a method for blind tip estimation where the accuracy of prediction depends on the actual sample features. If the features on the original sample surface are sharper than the tip geometry then the prediction is accurate else the algorithm only yields a close approximation of the tip geometry as shown below.

Morphological Operation of Open: The algorithm for blind tip estimation presented below utilizes simple grayscale morphological operations, namely dilation, erosion and opening. It is therefore necessary that we first present the mathematical equations used to perform these operations. More detailed information on Mathematical Morphology is available in Appendix A and all of the suggested references.

The set notation for dilation of set A by set B is:

$$A \oplus B = \bigcup_{\boldsymbol{b} \in B} (A + \boldsymbol{b}) \qquad \text{3-41}$$

The same result in terms of two dimensional surfaces is given by:

$$T[A \oplus B](x,y) = \max_{(x',y')}[a(x - x', y - y') + b(x', y')]$$

......................3-42

Similarly, erosion operation is defined as:

$$A \ominus B = \bigcap_{b \in B}(A - \boldsymbol{b})$$

.............................3-43

$$T[A \ominus B](x,y) = \min_{(x',y')}[a(x + x', y + y') - b(x', y')]$$

......................3-44

$\boldsymbol{T}[f]$ refers to the top surface of the solid represented by *f*. Another morphological operation that is frequently used in image processing applications is *opening*. This operator is a combination of dilation and erosion operators discussed above.

$$A \circ B = (A \ominus B) \oplus B \text{..............................3-45}$$

Some of the properties of opening are,

$$A \circ B = \cup\{B + \boldsymbol{y} | B + \boldsymbol{y} \subset A\} \text{..............................3-46}$$

$$(A \oplus B) \circ B = A \oplus B \text{..............................3-47}$$

Estimation of probe geometry: The imaging process is modeled as the dilation of true sample surface by the reflected surface of probe used for scanning. Assuming $\boldsymbol{P}$ (same as $\boldsymbol{rt(x,y)}$ used in the reconstruction process) to be the reflected probe surface

$$I = S \oplus P \quad \text{3-48}$$

We know from the properties of the morphological dilation operator [Appendix A] that:

$$P \oplus I = I \oplus P = I \quad \text{3-49}$$

$$P \subseteq (P \oplus I) \ominus I \quad \text{3-50}$$

Our objective is to estimate the maximum non-distorted tip, or in other words the largest/bluntest tip that could have produced the given AFM image without distorting the true sample profile. This gives an upper bound for the estimated tip shape.

Based on equation 3-50 it is safe to say that an upper bound (P_{nd}) for the tip shape can be obtained by eroding the image surface with itself.

$$P \subseteq P_{nd} = I \ominus I \quad \text{3-51}$$

Using equation 3-47 we have

$$I \circ P = I \quad \text{3-52}$$

So our task has been reduced to finding a surface that would satisfy the above equation. However it should be noted that this method essentially yields a solution P_t that satisfies equation 3-52 and further $P \subseteq P_t$. Further it should also be noted that if a surface P satisfies equation 3-52 then any translate of this would also satisfy the equation. This problem is eliminated by adopting the convention that the max value of z in P is 0 and that the coordinate of this max point is at the origin [Equation 3-53]. In other words we are forcing the apex of the reflected probe surface to be at the origin

$$P(0,0) = 0 \quad \text{3-53}$$

From equations 3-53 and 3-46 we have

$$I = I \circ P = \bigcup\{P + \boldsymbol{y} | P + \boldsymbol{y} \subseteq I\} \text{..............................3-54}$$

This means that no part of the translated tip should extend above the surface I or that every point on surface I should be contained in one or more translates of P.

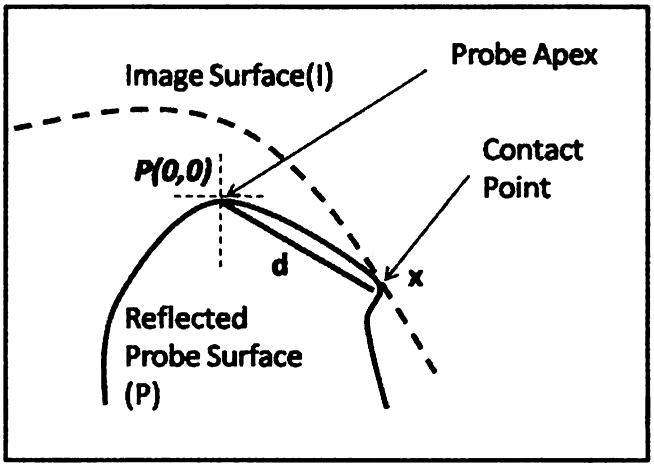

Figure 3-12 : Geometry of a reflected probe scanning the underside of an image surface

Figure 3-4 shows the reflected probe surface touching the image surface I at point $\boldsymbol{x}$ at a distance $\boldsymbol{d}$ from the probe apex. Since this distance would change as we move along the image surface we can assume it to be a function of $\boldsymbol{x}$. The translated tip can be represented by $(P + \boldsymbol{x} - \boldsymbol{d})$. Now based on the condition dictated by equation 3-54 we have

$$\forall\, \boldsymbol{x} \in I, \exists\, \boldsymbol{d} \in P \text{ such that } P \subseteq I + \boldsymbol{d} - \boldsymbol{x} \text{............................3-55}$$

Therefore we can use the above equation to exert an upper bound on the shape of the probe as it scans the underside of the image. However, we have no knowledge about ***d(x)*** since we do not know the actual point of contact between tip and sample surface for every value of $\boldsymbol{x}$.

We propose an iterative scheme that could be used to solve this problem. The sequence of steps is as follows

Step 1: we start with an initial estimate of P given by P_0. The point $\boldsymbol{d_0} \in P_0$ would replace the point $\boldsymbol{d}$ in equation 3-55.

Step 2: Modify P_0 to produce a smaller upper bound on the probe surface P_1 if the z component of $\boldsymbol{d_0}$ is greater than $\boldsymbol{d}$.

Step 3: Repeat the process till the estimated probe surface converges.

Though these steps seem simple, the absence of any a priori information about $\boldsymbol{d_0}$ makes the estimation process complex. We now derive all of the relevant mathematical equations that would help implement the above procedure on a computer. Let $\boldsymbol{P_0}$ be a right circular cylinder of radius much greater than the expected tip size but considerably lesser than the image size. Now at the ith iteration we have an estimate $\boldsymbol{P_i}$ for the reflected probe surface such that $P \subseteq P_i$ and we also know that P_i should satisfy equation 3-55 for some value of $\boldsymbol{d_i}$ $\forall \boldsymbol{x} \in I$.

Further, P is a subset of the *union* of probe shapes dictated by all possible values of $\boldsymbol{d_i}$. Now as seen in Figure 3.5 for a given value of $\boldsymbol{x} \in I$ we compute $(\boldsymbol{I} - \boldsymbol{x} + \boldsymbol{d_i}) \cap P_i$ to get a smaller upper bound on the probe shape and finally take a *union* of these for all possible values of $\boldsymbol{d_i}$. However there are some values of $\boldsymbol{d_i}$ that cannot be included while computing the *union* of shapes in the previous stage since these points cannot be the point of contact between the probe surface and image. For $\boldsymbol{d_i}$ values as shown in Figure 3.6 the probe apex lies outside the image surface and hence the revised volume does not have its apex at the origin. This implies that the condition given by equation 3-53 is not satisfied. Therefore while computing the union of shapes we consider $P_i'(x)$ which excludes the above mentioned $\boldsymbol{d_i}$ values. . Therefore $P_i'(x)$ can be mathematically expressed as follows:

$$P_i'(x) = \{\boldsymbol{d} | \boldsymbol{d} \in P_i \,\&\, 0 \in I - \boldsymbol{x} + \boldsymbol{d}\} \qquad \text{3-56}$$

Now considering all of the conditions that have been mentioned above we can represent the process of iteration by the following equation:

$$P \subseteq \bigcup_{\boldsymbol{d} \in P_i'(x)} [(I - \boldsymbol{x} + \boldsymbol{d}) \cap P_i] \qquad \text{3-57}$$

The above equation can now be rewritten as follows:

$$P \subseteq [(I - \boldsymbol{x}) \oplus P_i'(x)] \cap P_i$$

Now when we consider multiple points on the image surface we have

$$P \subseteq \bigcap_{\boldsymbol{x} \in I} [(I - \boldsymbol{x}) \oplus P_i'(x)] \cap P_i$$

Note that this is just a single step of iteration. When we implement the estimation algorithm using a computer we need to make use of the following expression:

$$P_{i+1}(x) = \min_{x' \in D_I} \left\{ \max_{d \in D_P} \{\min[i(x + x' - d) + P_i(d) - i(x'), P_i(x)]\} \right\}$$

Now on convergence we have

$$P_R = \lim_{i \to \infty} P_i$$

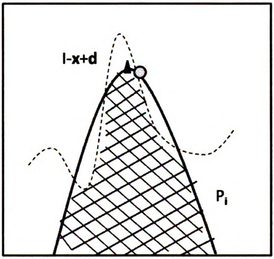

Figure 3-13 : Forcing a particular point on the surface of the reflect tip to touch the image.

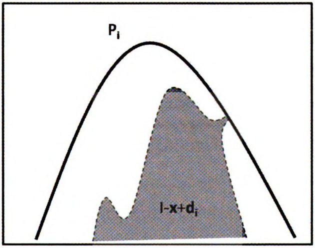

Figure 3-14 : Tip apex protruding beyond the image surface.

3.3.4 Summary & Results

The algorithms for performing Image Simulation, Surface Reconstruction and Blind Tip Estimation using Mathematical Morphology are summarized here.

Image Simulation

The procedure for computing the image surface $I(x,y)$, given the true sample surface ($S(x,y)$) and tip shape ($t(x,y)$) is as follows:

Step 1: First compute the reflected tip surface ($rt(x,y)$) given by:

$$rt(x,y) = -t(-x,-y)$$

Step 2: Dilate the sample surface ($S(x,y)$) by the reflected tip shape ($rt(x,y)$) using the relation:

$$I(x,y) = \max_{(x_a,y_a)} \left(S(x_a,y_a) + rt_{x_a,y_a}(x,y)\right)$$

$$= [S \oplus rt](x,y)$$

For the tip and sample surfaces shown in Figure 3-15 and 3-16, the image surface $I(x,y)$ obtained using the morphological operation of dilation is as shown in Figure 3-17. A profile comparison between the true sample surface and the AFM image surface is shown in Figure 3-18.

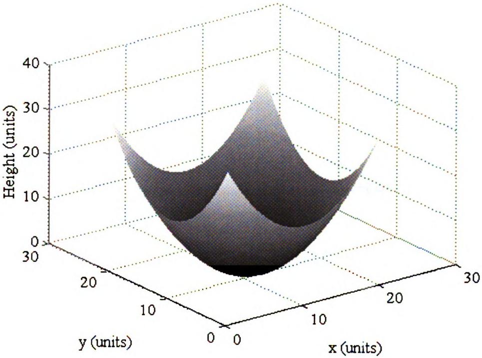

Figure 3-15 : Tip shape $t(x, y)$

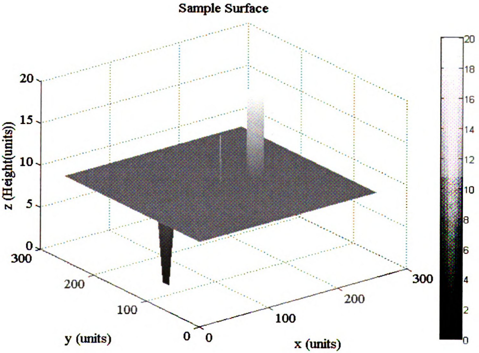

Figure 3-16 : True Sample Surface $S(x, y)$

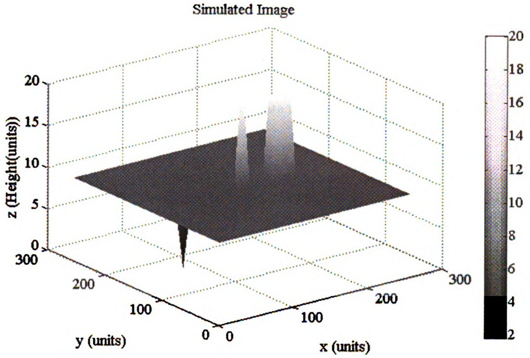

Figure 3-17: Simulated Image Surface $I(x, y)$

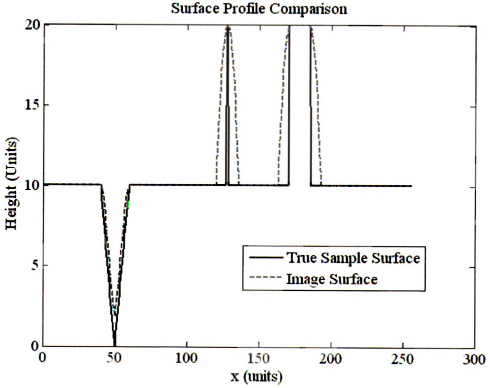

Figure 3-18 : Profile Comparison.

Surface Reconstruction and Certainty Map

Given the Image Surface ($I(x, y)$) and the tip shape ($t(x, y)$):

Step 1: Perform erosion of the image surface with the tip given by:

$$R(x, y) = \min_{(x_a, y_a)\epsilon D_I} (I(x_a, y_a) + t_{x_a y_a}(x, y))$$

$$R(x, y) = [t \ominus I](x, y)$$

Figure 3-19 shows the result of surface reconstruction obtained using the image and tip surface shown in Figure 3-17 and 3-15 respectively.

Step 2: Assign a certainty of 1 to point (x, y) on the reconstructed image surface only if the following condition is satisfied:

$\forall(x, y)\epsilon D_R$ if $\exists(x_1, y_1)\epsilon D_I$ such that

$R(x, y) = I(x_1, y_1) + t_{x_1 y_1}(x, y)$ and $\forall(x_2, y_2)\epsilon D_R$ and $(x_2, y_2) \neq (x, y)$

$$R(x_2, y_2) \neq I(x_1, y_1) + t_{x_1 y_1}(x_2, y_2)$$

Figure 3-20 shows a profile comparison of the true sample surface, image surface and the reconstructed sample surface along with the associated certainty map.

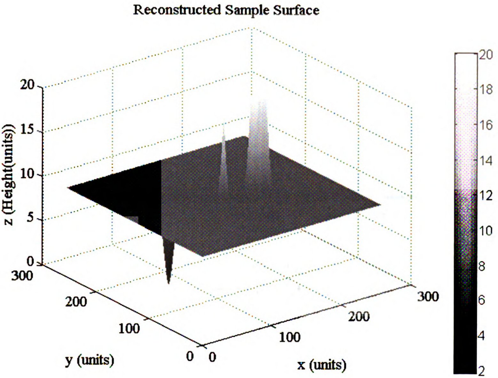

Figure 3-19 : Reconstructed sample surface.

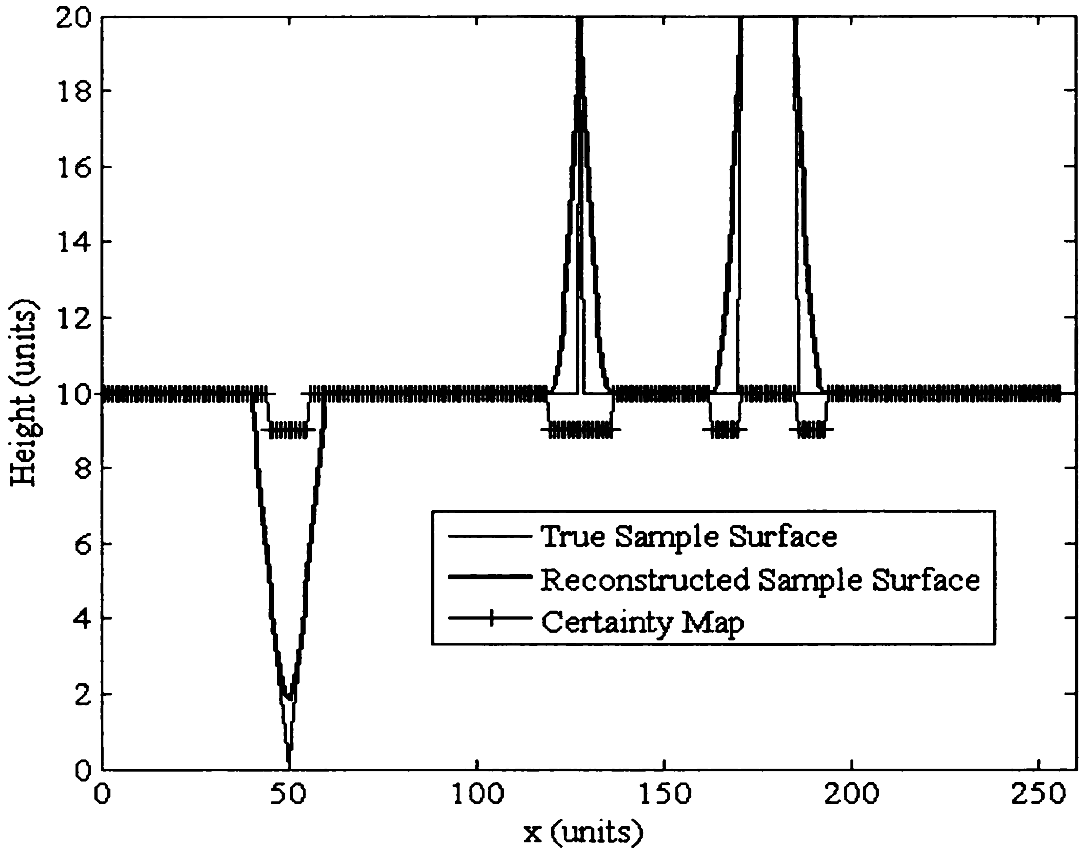

Figure 3-20 : Profile comparison with certainty map.

Blind Tip Estimation

Given the image surface $I(x, y)$ a blind estimate of the tip shape can be obtained using the following steps:

Step 1: Choose an initial estimate for the tip shape P_0. This is usually a zero matrix with dimension more than the original tip size but small when compared to the image size. Assign current tip estimate $P_i = P_0$.

Step 2: Now determine locations $\boldsymbol{x_i}$ on the image surface that would have maximum information about the tip shape.

Step 3: For each $\boldsymbol{x_i}$ find an upper bound on the tip shape by considering the union of translates given by

$$P \subseteq \bigcup_{d \in P_i'(x)} [(I - \boldsymbol{x} + \boldsymbol{d}) \cap P_i]$$

where $\quad P_i'(x) = \{\boldsymbol{d} | \boldsymbol{d} \in P_i \ \& \ 0 \in I - \boldsymbol{x} + \boldsymbol{d}\}.$

Step 4: Repeat Step 3 for all values of $\boldsymbol{x_i}$.

Step 5: Compute the intersection of possible tip shapes obtained from every image coordinate $\boldsymbol{x_i}$ given by

$$P \subseteq \bigcap_{x \in I} [(I - \boldsymbol{x}) \oplus P_i'(x)] \cap P_i$$

Or

$$P_{i+1}(x) = \min_{x' \in D_I} \left\{ \max_{d \in D_P} \{\min[i(x + x' - d) + P_i(d) - i(x'), P_i(x)]\} \right\}$$

Step 6: Use the new tip estimate P_{i+1} as the current estimate P_i and repeat steps 2 through 6 till the tip shape converges i.e.

$$P_R = \lim_{i \to \infty} P_i$$

Figure 3-21 shows the tip estimates at different stages of the blind tip estimation process using the impulse feature (A) in the image surface shown in Figure 3-17. The normalized mean square error between the estimated tip surface and the true tip surface is 1.0028. from Figure 3-22, we see that the estimate of the tip surface is accurate with a large error in the prediction of tip height. This can be attributed to the small height of the feature used for blind tip estimation. An accurate estimate of the tip shape requires that the sample surface have sharp features imaged by the tip. This estimation process would yield an accurate prediction if the image were to have local maximas that would yield accurate information about the tip shape. Since we try to find the bluntest tip for any given image point, using a blunt feature on the image would not yield an accurate estimate for the tip shape. The size of the initial estimate would make a difference to the accuracy of the prediction only if the size is small when compared to the image feature being considered.

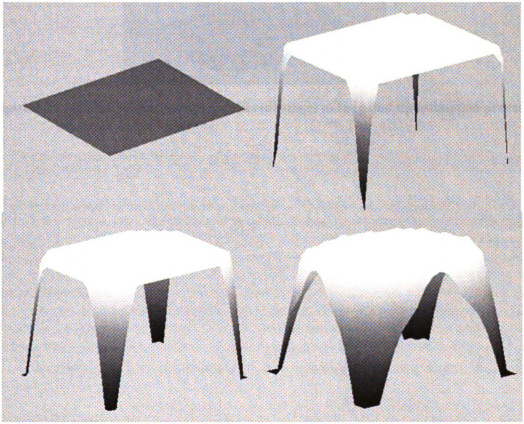

Figure 3-21: Tip estimates at different stages of the blind tip estimation process.

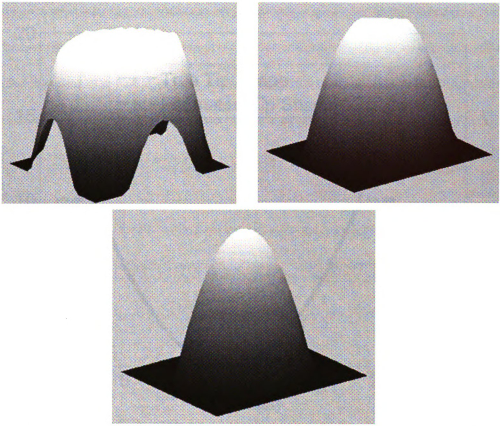

Figure 3-21 : (contd.) Tip estimates at different stages of the blind tip estimation process.

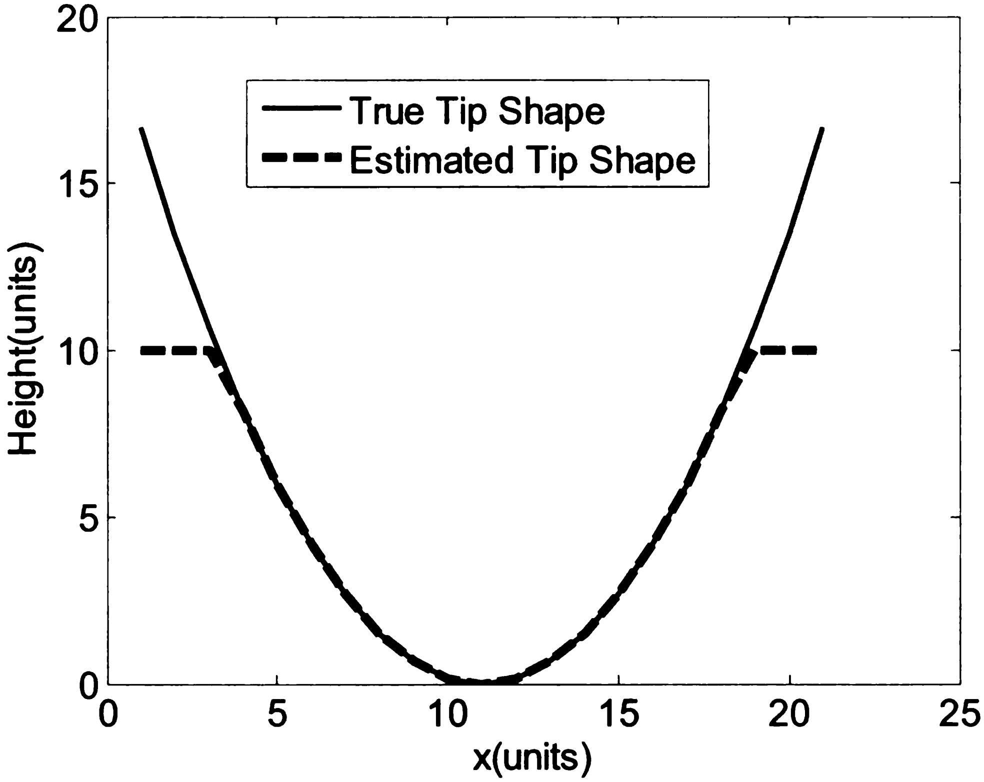

Figure 3-22 : Comparison between the true tip shape and the estimated tip shape.

Figure 3-23 and 3.24 shows the performance of the Mathematical Morphology based reconstruction algorithm on a sample with features very close to each other. It can be seen that the lateral resolution is greatly limited by the tip shape. A broad tip can cause two features that are close by to fuse into a single feature after imaging and reconstruction. Figure 3-25 showcases the thinning effect caused by improper tip shape selection. The information about depth of the trench as seen in the true sample surface is completely lost after imaging and reconstruction.

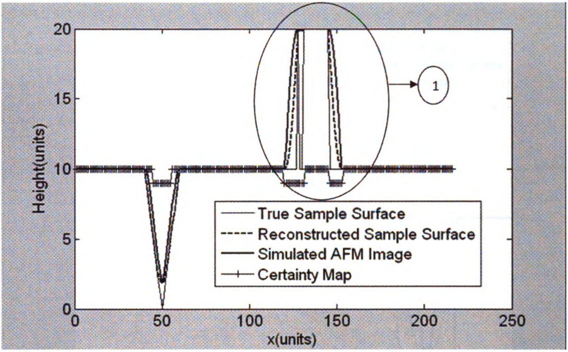

Figure 3-23 : Surface profile comparison: Really close features on the sample surface seem fused in the reconstructed surface

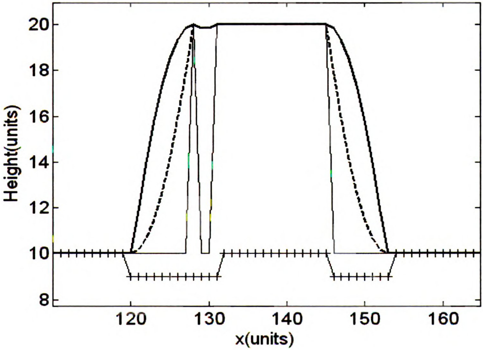

Figure 3-24 Zoomed in version of section 1 in Figure 3-23

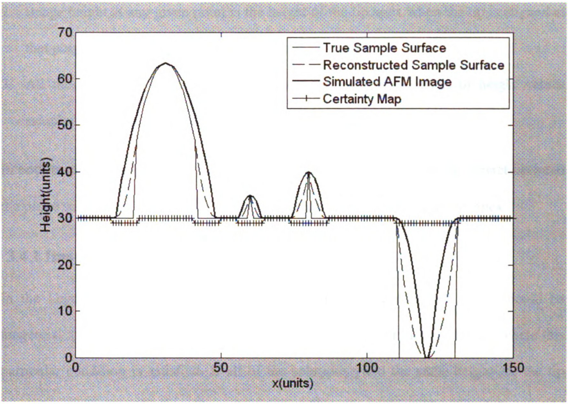

Figure 3-25 : Surface profile comparison: Thinning effect caused by tip shape.

3.4 Mathematical equivalence between the Mathematical Morphology and Legendre Transform based Reconstruction Methods.

We will now show that although the two methods approach the problem from different perspectives, namely, set-theoretic and transform-based, they are equivalent from a purely mathematical point of view.

Both the approaches make the following assumptions while developing their respective mathematical models,

1. At every point on the sample surface during the process of imaging the probe surface is in contact with the sample at least at one point without any penetration or compression.

2. Image height at any given point is the height of the tip apex when the tip is aligned at that point without violating assumption 1.
3. All the associated surfaces are represented by rectangular arrays of height values sampled at discrete intervals.

In both methods when the tip is at x, we first solve for the true point of contact between the probe surface and the sample, before we determine the height of the tip apex.

3.4.1 Image Simulation

In the Legendre Transform approach we know that the sample and probe should be tangential at the point of contact and hence we try to solve for all coordinates where this particular condition is satisfied. If all of the solutions yield the same height for the tip apex then we go no further. If we have a conflict where the different solutions yield different values for the image height we choose the one that yields the maximum height. From equation 3-4 we have

$$i(x') = \max\left(s(\boldsymbol{x}_j) - t(\Delta\boldsymbol{x}_j)\right) \quad \forall x_j$$

Now comparing this equation with the one used in the morphological method for image simulation, equation 3-28,

$$I(x,y) = \max_{(x_a,y_a)}\left(S(x_a,y_a) - t_{x,y}(x_a,y_a)\right)$$

$$i(\boldsymbol{x}) = \max\left(s(\boldsymbol{x}_a) - t(\Delta\boldsymbol{x}_a)\right) \forall \boldsymbol{x}_a \qquad \text{3-58}$$

Where $i(\boldsymbol{x}) = I(x,y); s(\boldsymbol{x}_a) = S(x_a,y_a); t(\Delta\boldsymbol{x}_a) = t(x_a - x, y_a - y)$ & $\boldsymbol{x} = (x,y)$

Equation 3-58 is same as the equation used in the Legendre Transform (LT) method after the first step of elimination. Therefore equation 3-58 is equivalent to the second step of elimination adopted in the LT method. However, it should be noted that the coordinates $\boldsymbol{x_j}$used in equation 3-4 are a subset of the coordinates $\boldsymbol{x_a}$used in equation 3-58. Since the coordinates $\boldsymbol{x_j}$ were obtained after checking for the condition that the probe surface was tangential to the sample. It should be noted that even though the morphological methods contain more number of points during its test for the maximum height these additional points will not yield the maximum value due to the fact that the probe surface is not tangential to the sample at these locations. This means that around the neighborhood of **x** the separation between the two surfaces varies in that some points in the neighborhood have lesser separation while the others have larger separation. This concept would become clear if we take a look at the constraints imposed in the morphological method that resulted in equation 3-28.

Constraint 1: In contact mode at every image the probe surface touches the sample surface at least at one point [Equation 3.25].

Constraint 2: Corresponding to every image point in contact mode imaging the probe height at every point is always greater than or equal to the sample surface height at the corresponding point [Equation 3.26].

The above stated constraints clearly ensure that the sample surface and probe are tangential at the point of contact. In summary, the contact points eliminated by the Legendre Transform method's tangent criterion are the same as those eliminated by Morphological method's constraints and hence both methods should definitely yield the same result for image simulation.

3.4.2 Surface Reconstruction

In the LT method the fundamental equation for surface reconstruction is given by

$$\Delta x(x') = x - x'$$

$$s(x) = i(x') + \Delta s(x') \quad \text{.................................3-59}$$

Given the probe surface $t(\Delta x)$ and image surface $i(x')$, Keller uses the relation $di/dx' = dt/d\Delta x$ to find Δx in terms of x' using which he computes $\Delta s(x')$ using the relation

$$\Delta s(x') = t(\Delta x(x'))$$

Substituting this in equation 3-59 we obtain the true sample surface.

In the case of a given point $[(x_1, y_1) \in D_I]$ on the image surface once the actual contact point $[(x, y) \in D_S]$ is first computed and the true sample surface height is retrieved using the relation

$$s(x, y) = i(x_1, y_1) + t(x - x_1, y - y_1)$$

In the morphological method the approach used to find the true point of contact is given by equation 3-33 with constraint imposed by equation 3-31 which ensures that the surfaces are tangential at the point of contact. The difference between the two approaches is that one uses an exact inverse operation (inverse Legendre Transform (ILT)) while the other uses erosion which is not the inverse of dilation but a dual operator. The ILT yields holes in the reconstructed image because of the fact that LT is a many to one mapping. Mathematical morphology also yields values of the surface height with zero certainty. However at the locations where both methods ensure 100% certainty the results provided by the two methods are the same. This is because both deconvolution procedures use exact inverse of the image simulation transform and since the image simulation transforms are equivalent the reconstruction transforms are also equivalent.

For the tip shape presented in Figure 3-6 and Sample Surface as shown in Figure 3-26 below, the image surface would be given by Figure 3-7. Figure 3-27 draws a comparison of surface profiles between the sample surfaces reconstructed using the Legendre Transform method the one obtained using Mathematical Morphology along with the associated certainty map.

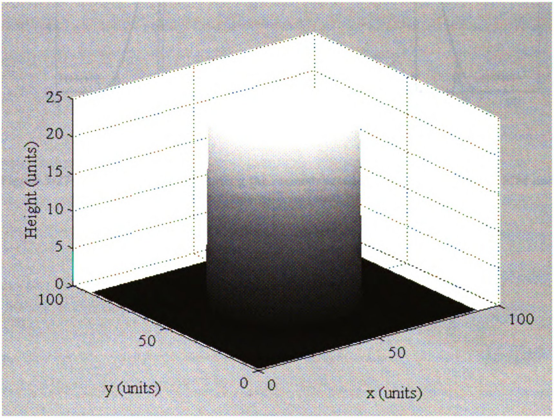

Figure 3-26 : Sample Surface.

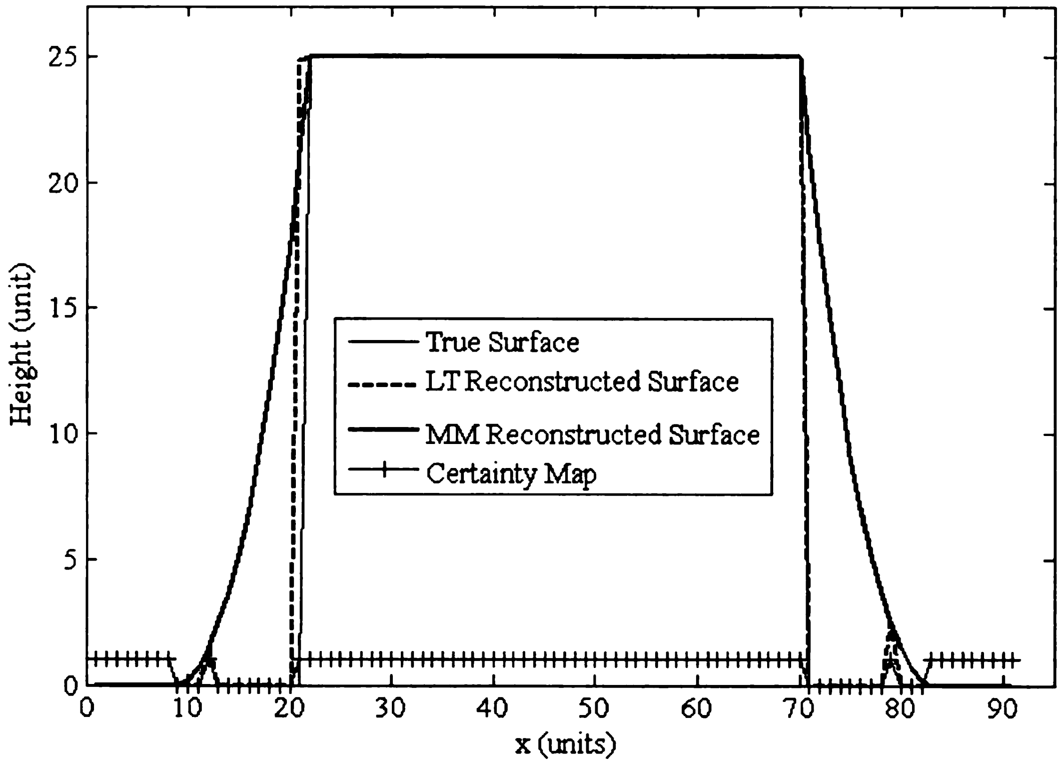

Figure 3-27 : Surface Profile comparing the reconstructed surface obtained using MM and LT methods with certainty map.

Chapter 4 Deconvolution of AFM data in Nanobiology.

The family of scanning probe techniques has revolutionized the study of nanostructures. The potential use of SPM in biological studies was apparent right after its invention in the early 1980s owing to its extremely high resolution. The Scanning Tunneling Microscope (STM), first in the SPM family, was limited by the fact that it could only be used to image conductive matter or thin layers of organics but this was overcome with the invention of the Atomic Force Microscope. The development of AFM opened new perspectives for the investigation of surfaces with high lateral and vertical resolutions. Within a few years scientists realized that other than its potential use as a high resolution microscope an AFM system could also be used for spectroscopic analysis, surface modification and molecular manipulation (33) , this increased the realm of AFM use. After the invention of the pico-newton systems, AFMs are now being used as a tool to study inter and intra molecular forces and to evaluate and characterize mechanical properties of biological samples such as: topography, elasticity and adhesive properties owing to its high sensitivity.

The AFM system has a number of advantages appealing to biological applications:

1. The ability to image non-conductive samples.
2. Ability to image soft biological tissues without damaging it.
3. It requires very little sample preparation when compared to the SEM or TEM.
4. Its ability to operate in a variety of environmental conditions such as ambient air, liquid and vacuum.

5. Liquid medium helped reduce Van der Waals and surface adhesive force which allowed biological investigations at near life like conditions.

All of these features helped utilize the AFM system to achieve a number of firsts in the field of nanobiology:

- First direct observation of DNA and RNA
- First direct investigation of membrane protein.
- First direct investigation of ligand binding by functionalized tip.

Biomolecules, proteins, DNA, cells and tissues are some of many biological samples of interest studied using AFM. Not only structural properties can be investigated, but also mechanical or chemical and functional properties are the focus of many AFM applications.

The main drawback with the AFM system is that it requires complementary imaging techniques to provide subsurface information in biological samples. Further, AFM images are plagued by artifacts produced by finite size of the probe tip. In the following section we present the application of deconvolution techniques discussed in the previous chapter to obtain accurate measurements of features in biological samples imaged using an Atomic Force Microscope.

4.1 Application of AFM to the study of Polymer Nanofibers.

The process of electrospinning (34) is a complicated combination of polymer science, electronics and fluid mechanics used to produce polymer nanofibers with diameters in the range of 50-500nm. These nanofibers are of substantial scientific and commercial interest in biomedical applications. In addition to the wide gamut of applications for nanofibers the new non-woven fabrics made of polymer nanofibers are being researched to be novel scaffold for cell growth. The morphology and properties of nanofibers limits its use as a functional material. Therefore the study of these properties to identify biocompatible carbon-based structures for tissue scaffold applications is of great interest.

Tissue scaffolds that allow the re-growth of cells into damaged areas are of great medical importance. Rigidity (elasticity), surface roughness, local chemistry, and curvature are all known to trigger cell responses (35). Nowadays Atomic Force Microscopes are being widely used to study these properties but in order to achieve its full potential for biological investigations there is a need to integrate signal processing techniques with AFM. In this section we focus on the use of deconvolution techniques to help improve the accuracy of an AFM to predict the curvature of an electrospun polymer fiber.

Figure 4-1 shows three images of polymer fiber nets obtained using an Atomic Force Microscope operating in the contact mode. Before estimating the fiber curvature it is necessary to apply mathematical morphology based reconstruction to the samples to remove any tip artifacts that maybe present.

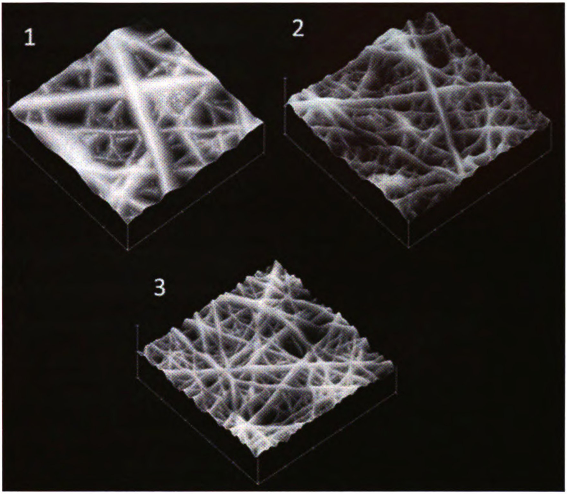

Figure 4-1: Polymer nanofibers samples images using AFM

4.1.1 Results of Tip Shape Estimation

As seen earlier the reconstruction process requires that the tip shape be known. Figure 4-2 shows the shape of the tip as per manufacturer's datasheet specifications (Pyramidal with base size 2.5nm x 2.5nm), but it is well known that the tip shape undergoes changes with repeated use. A blind estimate of the tip shape was obtained from samples 1 and 2. The initial estimate was chosen to be a zero matrix of size .3um x .3um. Figure 4-3 shows a comparison between the estimated and manufacturer specified tip shapes. The error between the estimate and the manufacturer's tip shape for samples 1 and 2 are 0.1264 and .0039 respectively.

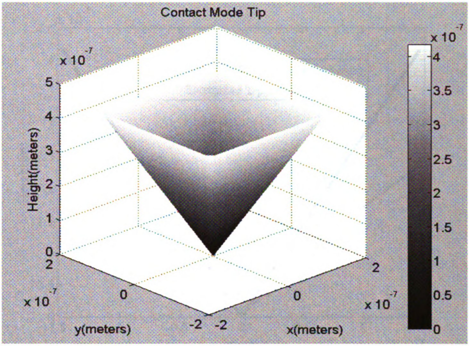

Figure 4-2 : Tip shape based on manufacturer's specification

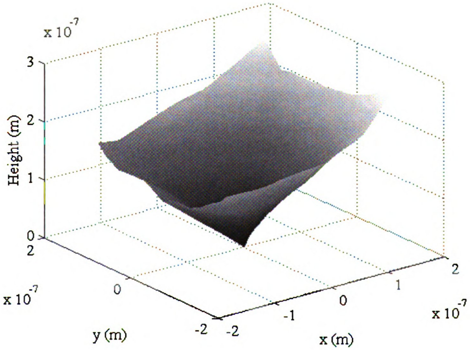

(a)

Figure 4-3: Blind estimate of tip shape obtained using (a & b) Sample 1 (c & d) Sample 2

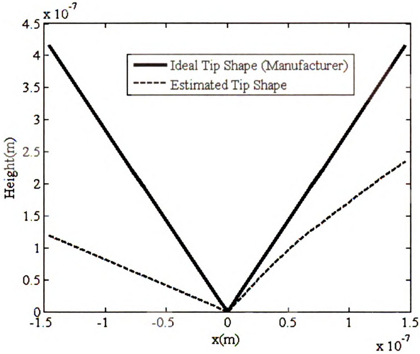

(b)

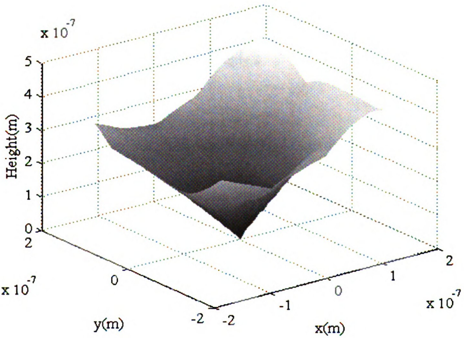

(c)

Figure 4-3: (contd.) Blind estimate of tip shape obtained using (a & b) Sample 1 (c & d) Sample 2

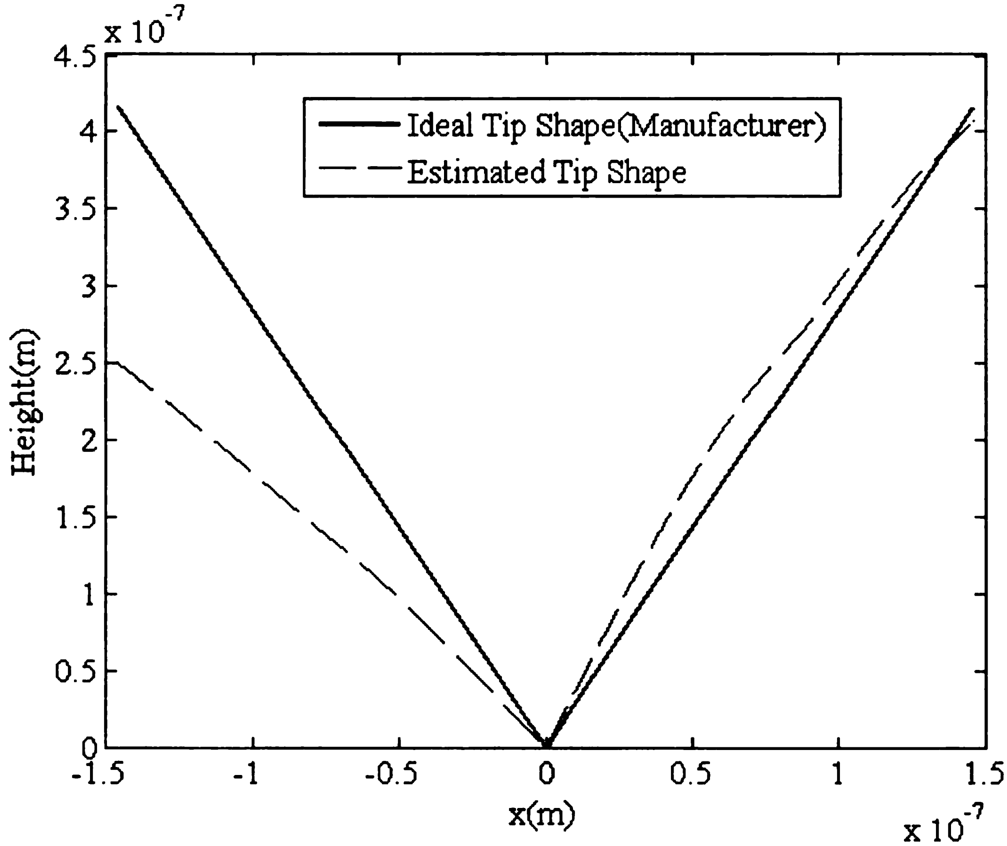

(d)

Figure 4-3 : (contd.) Blind estimate of tip shape obtained using (a & b) Sample 1 (c & d) Sample 2

4.1.2 Results of Deconvolution

The three sample surfaces were reconstructed using the manufacturer specified tip. The results after reconstruction are as shown in Figure 4-4. Specific fibers were selected from samples 2 and 3 after reconstruction and an estimate of their curvatures were obtained using the Kasa Circle Fit (36; 37). The procedure is simple [Figure 4-5]:

- Select a particular fiber cross section from the sample.
- Select a portion of this cross section that is to be passed as input to the circle fit algorithm.
- Obtain the diameter of the selected fiber using the Kasa Circle Fit Algorithm.

Figure 4-6 shows a histogram of fiber widths obtained using 26 fibers selected from samples 2 and 3. It is seen from Figure 4-6 that the majority of the fiber widths lie between 50 and 200nm.

In order to achieve a more accurate estimate for the fiber diameter, the sample surfaces were deconvolved using the estimated tip shapes. The diameters for the 26 fibers were then obtained using the procedure outlined above. Figure 4-7 shows the reconstructed surface profiles for the three samples. In figure 4-8 it can be seen that the diameter of the majority of fibers still falls between 50 and 200 nm. The similarity of these results clearly indicate that the blind tip estimation procedure yields a tip shape that is very close to the manufacturer specified tip shape.

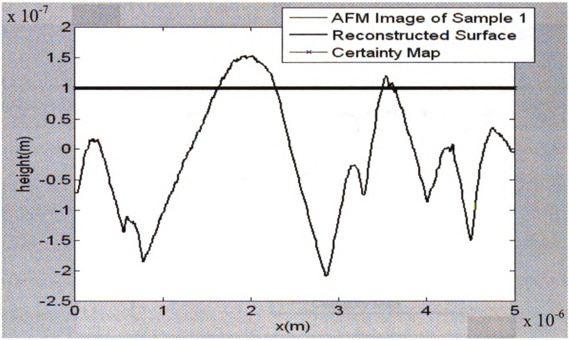

(a)

Figure 4-4: Reconstructed surface profiles for (a) Sample 1 (b) Sample 2 (c) Sample 3 obtained using manufacturer's tip shape.

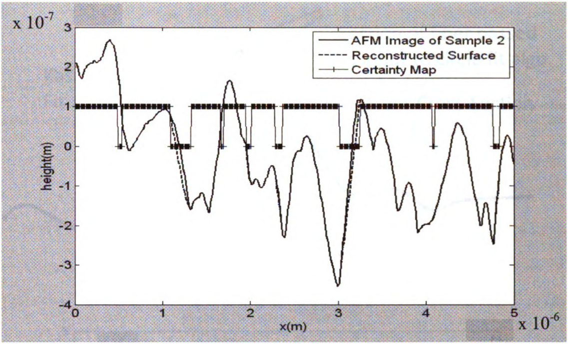

(b)

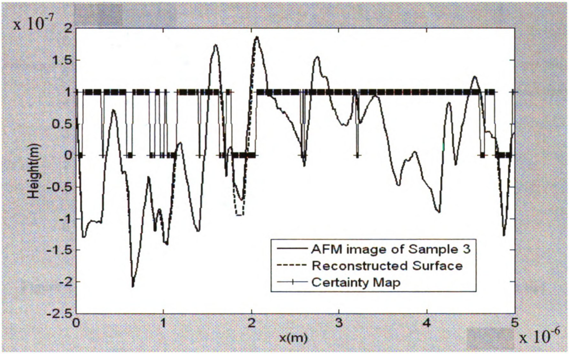

(c)

Figure 4-4 : (contd.) Reconstructed surface profiles for (a) Sample 1 (b) Sample 2 (c) Sample 3 obtained using manufacturer's tip shape.

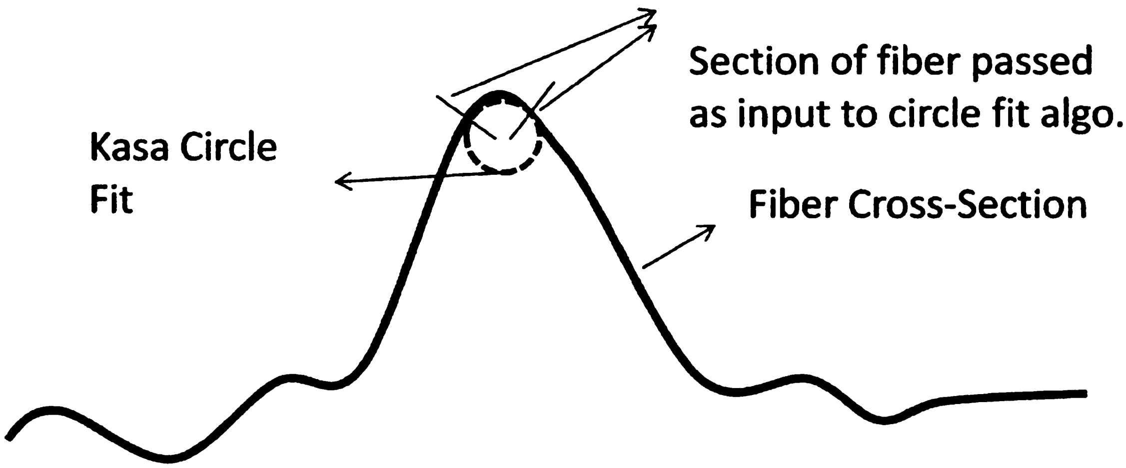

Figure 4-5: Kasa Circle Fit

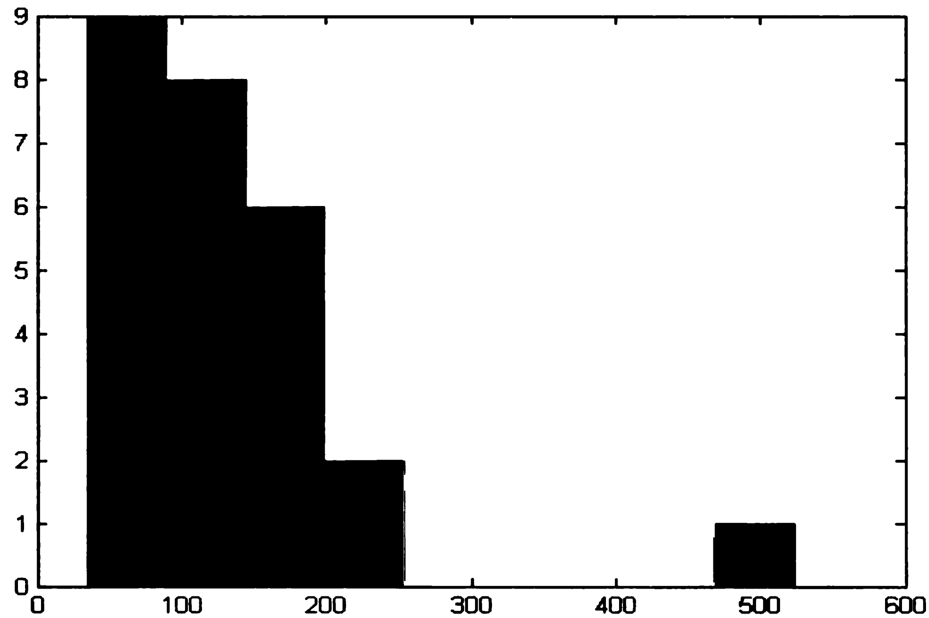

Figure 4-6: Histogram of Fiber Width Estimates (Obtained using manufacturer's tip)

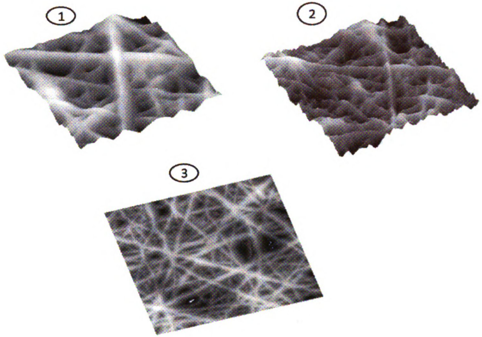

Figure 4-7 : Reconstructed Sample Surface (1) Sample 1 (2) Sample 2 (3) Sample 3

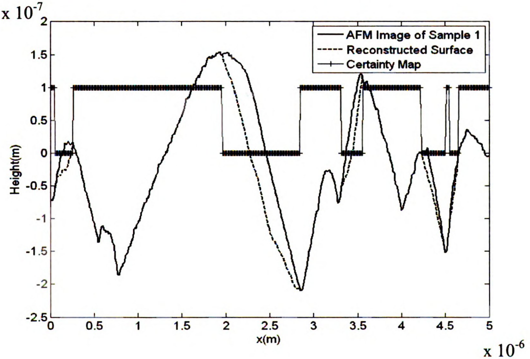

(a)

Figure 4-8: Reconstructed Surface Profiles obtained using estimated tip surface.

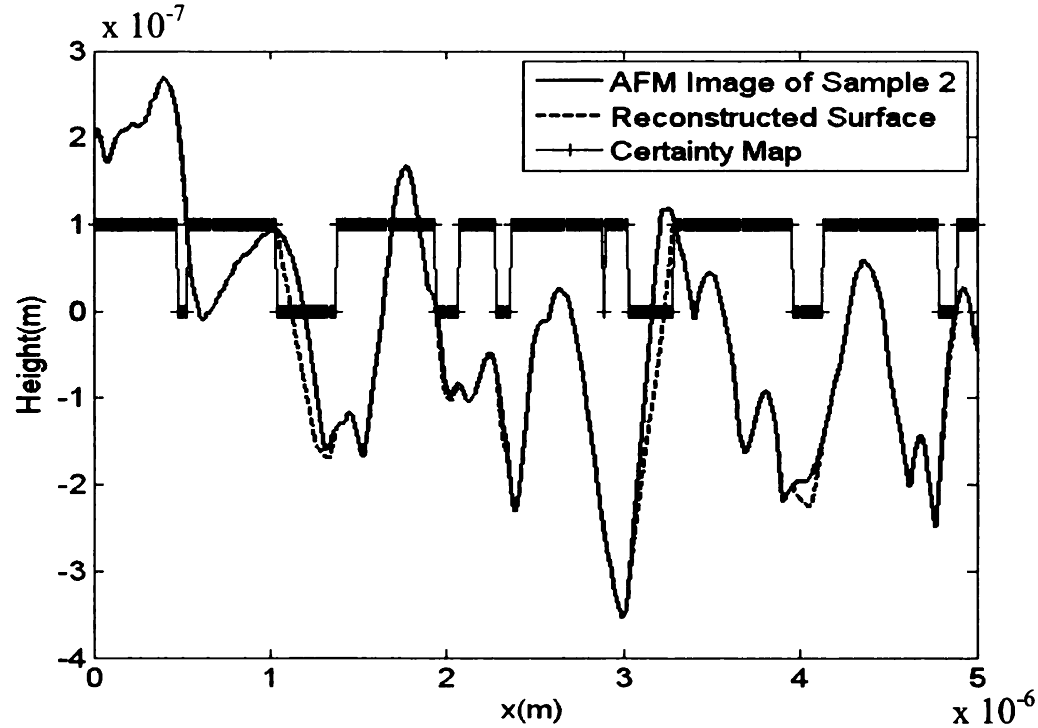

(b)

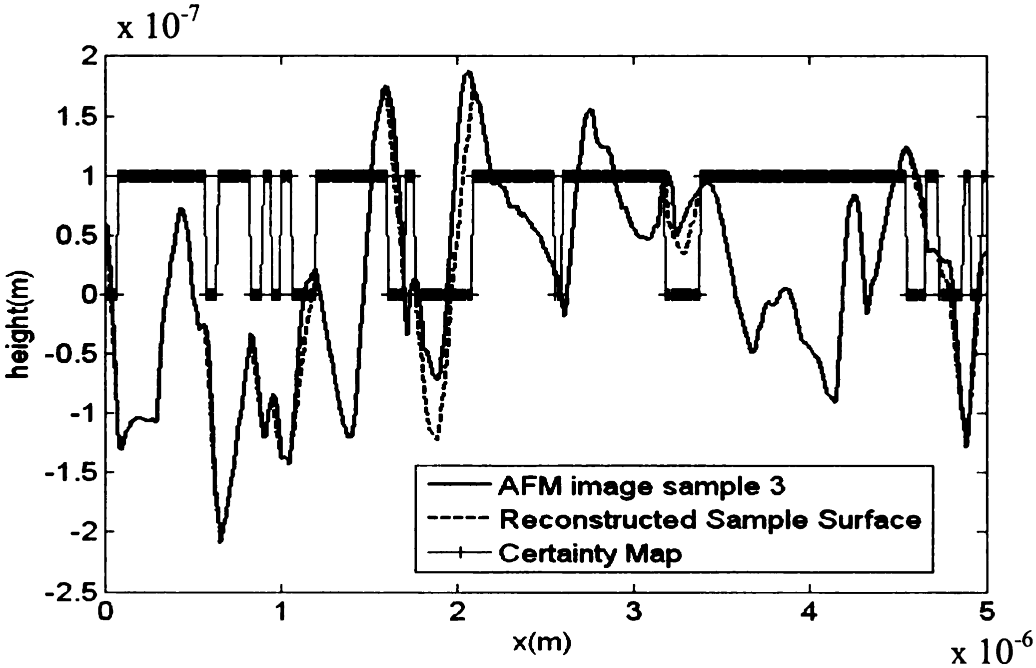

(c)

Figure 4-8: (Contd.) Reconstructed Surface Profiles obtained using estimated tip surface.

Table 4-1 Fiber width estimates in nanometers.

1	2	3	4	5	6	7	8	9	10
119.5	136.5	67.6	295.1	68.79	185	121.77	57.8	174.7	91.3
11	**12**	**13**	**14**	**15**	**16**	**17**	**18**	**19**	**20**
98.4	116.5	148.36	98.4	161.4	519.11	276.52	73.8	50.4	153.13
21	**22**	**23**	**24**	**25**	**26**				
266.5	320.1	122	112.3	312.1	414.6				

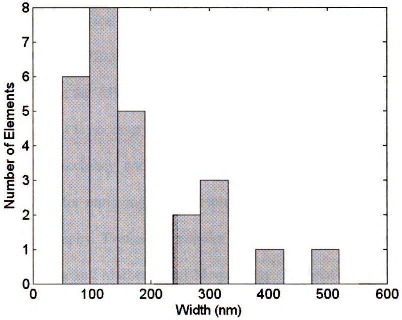

Figure 4-9 : Histogram of fiber width estimates.

Figure 4.5 shows that most of the polymer fibers in the given sample set have a fiber diameter between 50:200nm.

Chapter 5 Conclusion and Future Work

Atomic force microscope belongs to the family of scanning probe microscopy (SPM) techniques that are used in the field of nanotechnology to image surface topography at the nano scale by mechanically probing the surface. Atomic Force Microscopes can be used to image both conductive and non-conductive samples and works well in ambient air, liquid and vacuum. Owing to the pico-newton force exerted on the sample an AFM can be used to make nanobiological investigations under life like conditions. The accuracy of measurements in AFM is affected by the shape of the tip used to image the sample. This introduces distortions in the AFM image which should be eliminated prior to interpreting the AFM data. Hence, it is necessary to integrate signal processing techniques with AFM to increase both the accuracy and reliability of data. Deconvolution algorithms are proposed as a method for removing artifacts introduced by tip shape and reconstructing the true surface topography. Two of the popular techniques for deconvolution are based on Legendre Transform and Mathematical Morphology. The mathematical model based on Legendre Transforms defined using continuous analytic functions is more intuitive and easy to understand. However in practical applications where the surfaces are complex numerical implementation of Legendre Transform is rather cumbersome. In contrast, Mathematical morphology based reconstruction is nonlinear and more complex but is easy to implement using a computer. It also provides additional features such as certainty maps and blind tip estimation that aid in image analysis. In practical situation, the true tip size is seldom known and hence the availability of a blind tip estimation model is invaluable.

Although the two algorithms approach the deconvolution problem from different angles, this thesis shows that both algorithms are equivalent from a purely mathematical point of view and the choice of one over the other is a personal preference.

The study of polymer nanofibers is necessary for many biological applications and Atomic force microscopy is a very useful tool to study the different properties of the nanofibers such as elasticity, roughness and curvature. In this thesis it has been shown that the curvature of the polymer nanofibers can be predicted accurately with the help of deconvolution algorithms applied to Atomic Force Microscope data.

Several improvements can be made to the existing deconvolution methods. In all of the algorithms discussed in this thesis the effect of other types of noise has not been taken into consideration. It is necessary to design filters specific to an application before using any given deconvolution technique. Reconstruction algorithms can be improved by including a model of the probe and cantilever mechanics that leads to tip artifacts. Different modes of AFM provide different and unique type of information. Data fusion techniques that combine the different pieces of information in a synergistic manner should be investigated. All of this information can be used to get a a more accurate estimate of sample surface features. . The curvature estimates for the polymer nanofibers obtained using AFM can be used further to yield a more accurate reconstruction of the sample surface. The AFM image can be eroded further using a tip with radius of curvature equal to the average value obtained above. Once an accurate estimate of the fiber diameter is obtained the last step would be to establish a correlation between the curvature of the fiber and cell re-growth.

Appendix A: Mathematical Morphology

Morphological image processing (38) is used widely for extracting components or features of objects in an image. The language of mathematical morphology is based on set theory. Sets in mathematical morphology are used to represent objects in n-dimensional Eucledian space. While dealing with binary images each element of the set is a 2-tuple comprising coordinates of a black/white pixel in the image. While dealing with gray scale images the elements of the set represents the gray level value of each pixel in an image.

Basic concepts of set theory such as union, subset, intersection, mutual exclusivity, translation, complement and difference are used for defining operations in mathematical morphology. This tutorial explains the basic operations of image dilation and erosion for gray scale images using simple set theoretic operations such as union, intersection and translation. Translation of a set **S** by a vector **d** is obtained by adding **d** to every element of **S**:

$$S + \boldsymbol{d} = \{\boldsymbol{s} + \boldsymbol{d} | \boldsymbol{s} \in S\}$$

This has been illustrated graphically in the **Figure A1(a)** where the object represented by set S is translated by **d** $= (d_x, d_y)$. The top of the translated object, T[S+d] can be represented as follows:

$$T[S + \boldsymbol{d}](x, y) = s(x - d_x, y - d_y)$$

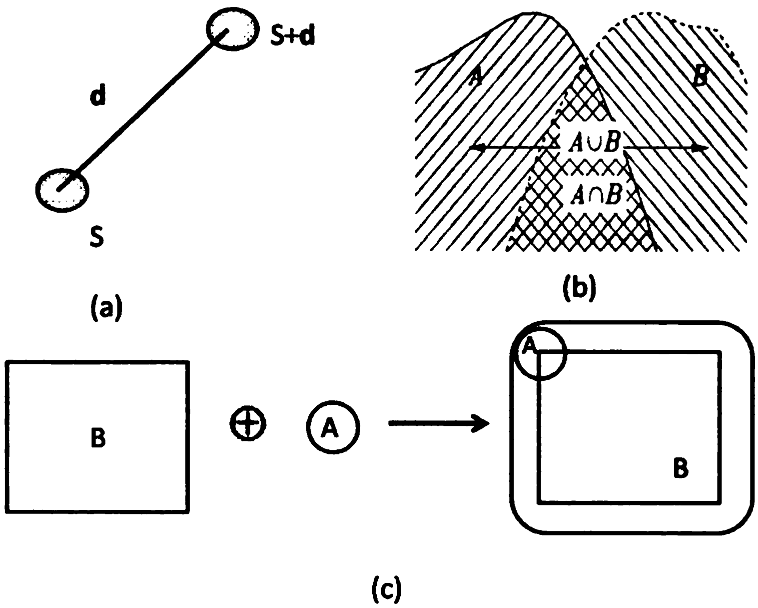

Figure A1: (a) Translation of a set S by a vector d (b) Union and Intersection of two sets (1)

(c) $A \oplus B$ **, Dilation of one set by another**

Similarly, the union of two objects A, B, illustrated in **Figure A1 (b)** is the maximum of the two tops T[A] and T[B] and the intersection refers to the minimum of the two tops. These can be expressed mathematically as

$$T[A \cup B](x,y) = \max\,[a(x,y), b(x,y)]$$

$$T[A \cap B](x,y) = \min\,[a(x,y), b(x,y)]$$

The morphological operation of dilation of an object B by a structuring element A is defined as

$$A \oplus B = \bigcup_{b \in B} (A + b)$$

The above expression is also interpreted as a union of translates as shown in **Figure A1(c)**. Here if we take the center of the circle A to be the point a = 0, dilation is the area swept by A as it is centered over every point b in B. In **Figure A1 (c)** the dilation of B by A is computed using the equation:

$$T[A \oplus B](x,y) = \max_{(u,v)}[a(x-u, y-v), b(u,v)]$$

The second fundamental morphological operation is Erosion. The erosion of a set A by B is defined as

$$A \ominus B = \bigcap_{b \in B}(A - b)$$

where '$\ominus$' represents the erosion operator. In grayscale morphology the expression is given by

$$T[A \ominus B](x,y) = \max_{(x',y')}[a(x+x', y+y') - b(x',y')]$$

Erosion can be thought of as the inverse of dilation. While dilation causes and object to grow erosion causes it to shrink as illustrated in **Figure A2**.

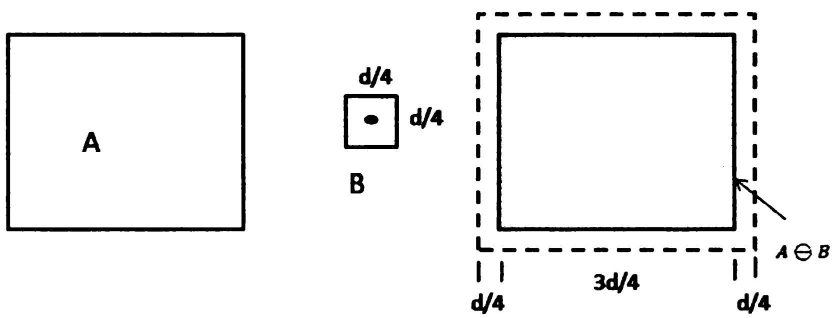

Figure A2: Erosion of A by B

More complex morphological operations such as 'Open' and 'Close' are obtained by combining dilation and erosion. . Opening of A by B is denoted by $A \circ B$ and is defined as

$$A \circ B = (A \Theta B) \oplus B$$

Closing of A by B is denoted by $A \bullet B$ and is defined as

$$A \bullet B = (A \oplus B) \Theta B$$

Appendix B: MATLAB Codes

Image Simulation: LT Method

```
x=[1:.2:50];
s=sin(.2*x); % Sample Surface
y=[1:.2:11];
t=.5*((y-6).^2)/16; % Tip Surface
temp=zeros(1,296);
s_new=temp;
ds=fix((cos(.2*x))*10000); % Slope of Sample Surface
dt=fix(((y-6)/8)*10000); % Slope along Tip Surface
temp(26:271)=ds;
s_new(26:271)=s;
for outer=26:271
   eq=(dt==temp(outer-25:outer+25)); % Elimination Process 1.
   s_sub=s_new(outer-25:outer+25);
   loc=find(eq==1);
   if(~isempty(loc))
      i(outer-25)=max(s_sub(loc)-t(loc)); % Elimination Process 2
   else
      i(outer-25)=max(s_sub-t); % i is the Image Surface
   end
end
```

Surface Reconstruction: LT Method

```
Reconstructed_Sample_Surface=zeros(size(Image_Surface))-5;
%---------Image Surface Size Computation--------%
 img_xsize=size(Image_Surface,2);
 img_ysize=size(Image_Surface,1);
 %---------------------------------------------%
 %---------Tip Size Computation------------------%
 tip_xsize=size(Tip_Surface,2);
 tip_ysize=size(Tip_Surface,1);
 %---------------------------------------------%
Big_Recon=zeros(img_ysize*2,img_xsize*2)-5;

Big_Recon(round(img_ysize/2+1):round(img_ysize*3/2),round(img_xsize/2+1):round(i
mg_xsize*3/2))=Image_Surface;
 %---------------------------------------------%
```

```
Big_Recon(round(img_ysize/2+1):round(img_ysize*3/2),1:round(img_xsize/2)) =
Image_Surface(:,1) * ones(1, round(img_xsize/2));

Big_Recon(round(img_ysize/2+1):round(img_ysize*3/2),round(img_xsize*3/2+1):(img_
xsize*2)) = Image_Surface(:,img_xsize) * ones(1, floor(img_xsize/2));

 Big_Recon(1:round(img_ysize/2),1:(img_xsize*2)) = ones(round(img_ysize/2),1 ) *
Big_Recon(round(img_ysize/2+1),:);

Big_Recon(round(img_ysize*3/2+1):(img_ysize*2),1:(img_xsize*2)) =
ones(floor(img_ysize/2),1 ) * Big_Recon(round(img_ysize*3/2),:);
%---------------------------------------------%
bimg_xsize=size(Big_Recon,2);
bimg_ysize=size(Big_Recon,1);
 %---------------------------------------------%
 Rt = 3;  %%% radius of the tip
 ix = diff(Big_Recon,1,1);
 iy = diff(Big_Recon,1,2);
 deltaix = fix(Rt.*ix(1:bimg_ysize-1,1:bimg_xsize-1));
 deltaiy = fix(Rt.*iy(1:bimg_ysize-1,1:bimg_xsize-1));
 deltas = (deltaix .^2 + deltaiy .^2)/(2*Rt) ;
  %---------------------------------------------%
  R = zeros(size(Big_Recon)-1);
  countt = zeros(size(Big_Recon)-1);
  for row= 1: size(Big_Recon,1)-1
          for col = 1:size(Big_Recon,2)-1
                  R(row + deltaix(row,col),col + deltaiy(row,col)) =  Big_Recon(row,col) +
                  deltas(row, col);
                   countt(row + deltaix(row,col),col + deltaiy(row,col)) = countt(row +
                  deltaix(row,col),col + deltaiy(row,col))+1;
                  counttt(row + deltaix(row,col),col + deltaiy(row,col)) = 1;
          end
 end
 countt = countt.*100;
count =
countt(round(img_ysize/2+1):round(img_ysize*3/2),round(img_xsize/2+1):round(img_x
size*3/2));

counttt0 =
counttt(round(img_ysize/2+1):round(img_ysize*3/2),round(img_xsize/2+1):round(img_x
size*3/2));

ix0 =
ix(round(img_ysize/2+1):round(img_ysize*3/2),round(img_xsize/2+1):round(img_xsize*
3/2));
```

```
iy0 =
iy(round(img_ysize/2+1):round(img_ysize*3/2),round(img_xsize/2+1):round(img_xsize*
3/2));
%%%%%% reconstructed true image
ts =
R(round(img_ysize/2+1):round(img_ysize*3/2),round(img_xsize/2+1):round(img_xsize*
3/2));
 save('.\Data\LT_Reconstructed_Sample_Surface.asc','-ascii','ts');
save('.\Data\LT_CMAP.asc,'-ascii','countttt0');
Reconstructed_Sample_Surface=ts;
```

Image Simulation: MM method

```
if(isempty(Tip_Surface))
    msgbox('Please select the Tip Surface to be used(Process -> Tip Selection)');
elseif(isempty(Sample_Surface))
    msgbox('Please select the Sample Surface to be used(Process -> Surface Selection
    Orig)');
else
     sim_img=zeros(size(Sample_Surface)); % Initializing Image Surface.
     temp=zeros(size(Sample_Surface,1)+(tip_ysize-1), size(Sample_Surface,2)
    +(tip_xsize-1)) - inf;

    temp(ceil(tip_ysize/2):size(temp,1)-floor(tip_ysize/2),ceil(tip_xsize/2):size(temp,2)-
    floor(tip_xsize/2))=Sample_Surface;

    index=0;
    h = waitbar(0,'Please Wait : Image Simulation underway.....');
     for row=ceil(tip_ysize/2):size(temp,1)-floor(tip_ysize/2)
       for col=ceil(tip_xsize/2):size(temp,2)-floor(tip_xsize/2)
            index=index+1;
            for r=-floor(tip_ysize/2):floor(tip_ysize/2)
               for c =-floor((tip_xsize/2)):floor((tip_xsize/2))
                     sum(r+ceil(tip_ysize/2),c+ceil(tip_xsize/2))=temp(row+r,col+c)-
                     Tip_Surface(r+ceil(tip_ysize/2),c+ceil(tip_xsize/2));
               end
            end
            sim_img(row-floor(tip_ysize/2),col-floor((tip_xsize/2)))=max(max(sum));
            waitbar(index/(sample_length*sample_width));
       end
    end
    close(h);
    save('./Data/Simulated_Specimen_Surface_sharp.asc','-ascii','sim_img');
    Simulated_Image=sim_img;
End
```

Surface Reconstruction: MM Method

```
%---------Image Surface Size Computation--------%
img_xsize=size(Image_Surface,2);
img_ysize=size(Image_Surface,1);
%---------------------------------------------%
%---------Tip Size Computation-----------------%
tip_xsize=size(Tip_Surface,2);
tip_ysize=size(Tip_Surface,1);
%---------------------------------------------%
P=Tip_Surface;
%---------------------------------------------%
 %---------Surface Reconstruction----------------%
Reconstructed_Sample_Surface=zeros(size(Image_Surface));
temp=zeros(size(Image_Surface,1)+(tip_ysize-1),size(Image_Surface,2)+(tip_xsize-
1))+inf;

temp(ceil(tip_ysize/2):size(temp,1)-floor(tip_ysize/2),ceil(tip_xsize/2):size(temp,2)-
floor(tip_xsize/2))=Image_Surface;
%---------------------------------------------%
index=0;
h = waitbar(0,'Please Wait : Surface Reconstruction Underway.....');
for row=ceil(tip_ysize/2):size(temp,1)-floor(tip_ysize/2)
    for col=ceil(tip_xsize/2):size(temp,2)-floor(tip_xsize/2)
        index=index+1;
         for r=-floor(tip_ysize/2):floor(tip_ysize/2)
                for c =-floor((tip_xsize/2)):floor((tip_xsize/2))
                        sum(r+ceil(tip_ysize/2),c+ceil(tip_xsize/2))=temp(row+r,col+c)+P
                        (r+ceil(tip_ysize/2),c+ceil(tip_xsize/2));
                end
        end
        Reconstructed_Sample_Surface(row-floor(tip_ysize/2),col-
        floor((tip_xsize/2)))=min(min(sum));

        waitbar(index/(img_xsize*img_ysize));
    end
end
close(h);
```

Blind Tip Estimation

```
function Blind_Tip_Estimation_Callback(hObject, eventdata, handles)
        global Simulated_Image;
    global Scanned_Data;
    global Estimated_Tip_Surface;
    % Initial Estimate for the tip Surface.
    tip_size=input('Please input the size of the tip to be estimated  :  ');
```

```
tip_est=zeros(tip_size);
    handlea=questdlg('Would you like to use the current simulated      image(else
   scanned data shall be used)???','','Yes','No', 'Yes');
if(size(handlea,2)==3)
   sim_img=Simulated_Image;
else
   sim_img=Scanned_Data;
end

% Get all sizes.
tip_ysize=tip_size;
tip_xsize=tip_size;
img_ysize=size(sim_img,1);
img_xsize=size(sim_img,2);
temp=zeros(img_ysize,img_xsize);
temp=sim_img;

% Waitbar Display to Show Progress.
index=0;
h = waitbar(0,'Please Wait : Blind Tip Estimation Underway.....');
for iter=1 %This is the number of iteration on all image points starting out with a
new estimate for tip shape.
   len=size([1],2);
   tip_iter(iter,:,:)=tip_est;
   len1=size([(tip_ysize+1):(img_ysize-(tip_ysize+1))],2);
   len2=size([(tip_xsize+1):(img_ysize-(tip_xsize+1))],2);
   for row=(tip_ysize+1):(img_ysize-(tip_ysize+1))
      for col=(tip_xsize+1):(img_ysize-(tip_xsize+1))
         for m=0:tip_size-1
            for n=0:tip_size-1
               index=index+1;
               dil=-inf;
               for r=0:tip_size-1
                  for c=0:tip_size-1
                     if((temp(row,col)-temp(row + floor(tip_size/2)-r, col +
                     floor(tip_size/2)-c))>tip_est(r+1,c+1))
                     else
                            tp=temp(row+m-r,col+n-c)+tip_est(r+1,c+1)-
                            temp(row,col);
                            dil=max(dil,tp);
                      end

                  end
                end
                if(dil==-Inf)
                      continue;
```

```
                else
                    if(dil<tip_est(m+1,n+1))
                        tip_est(m+1,n+1)=dil;
                    end
                end

            end
        end
        waitbar(index/(tip_ysize*tip_xsize*len1*len2*len));
      end
    end
  end
  close(h);
  Estimated_Tip_Surface=-fliplr(flipud(tip_est));
  save('.\Data\Estimated_Tip_Surface.asc','-ascii','Estimated_Tip_Surface');
```

Kasa's Circle Fit

```
function   [xc,yc,R,a] = f_circfit(x,y)
   x=x(:); y=y(:);
  a=[x y ones(size(x))]\[-(x.^2+y.^2)];
  xc = -.5*a(1);
  yc = -.5*a(2);
  R  =  sqrt((a(1)^2+a(2)^2)/4-a(3));
```

Bibliography

1. *Algorithms for Scanned Probe Microscope Image SImulation, Surface Reconstruction and Tip Estimation.* **Villarubia, J. S.** 4, 1997, Journal of Research of the National Institute of Standards and Technology, Vol. 102.

2. **Srleffler.** Scanning Probe Microscopy - History. *Wikipedia - The free encyclopedia.* [Online] November 2006. http://en.wikipedia.org/wiki/Scanning_probe_microscopy.

3. **Group, Condensed Matter Theory.** The Atomic Force Microscope. *Photonics Web Site.* [Online] Department of Physics, Imperial College London, August 17, 2004. http://www.sst.ph.ic.ac.uk/photonics/intro/AFM.html.

4. *Atomic Force Microscope.* **G. Binnig, C.F. Quate, Ch. Gerber.** 9, San Jose : The American Physical Society, March 3, 1986, Physcal Review Letters, Vol. 56, p. 530.

5. *Scanned Probe Microscopy - Current Status and Future Trends.* **Wickramasinghe, H. Kumar.** 1, New York : American Vacuum Society, January 1990, Journal of Vacuum Science & Technology A: Vacuum, Surfaces, and Films, Vol. 8, pp. 363-368. 1990JVST....8..363W.

6. **Wiesendanger, R.** Scanning Probe Microscopy and Spectroscopy: Methods and Applications. s.l. : Cambridge University Press, 1994.

7. *Deconvolution of Atomic Force Microscopy Data for Cellular and Molecular Imaging.* **Lalita Udpa, Virginia M. Ayres, Yuan Fan, Qian Chen, Shiva Arun Kumar.** 3, East Lansing : IEEE, May 2006, IEEE Signal Processing Magazine, Vol. 23, pp. 73-83. 1053-5888 .

8. **Li, Hong-Qiang.** Atomic Force Microscopy Student Module. *Atomic Force Microscopy.* [Online] April 24, 1997. http://www.chembio.uoguelph.ca/educmat/chm729/afm/firstpag.htm.

9. **Pacific Nanotechnology.** An Introduction to Atomic Force Microscopy Modes. *Pacific Nanotechnology Web Site.* [Online] http://www.pacificnano.com/afm-modes.html.

10. *Atomic Force Microscope - force mapping and profiling on a sub 100-A scale.* **Y. Martin, C.C.Williams, H.K. Wickramasinghe.** 10, New York : American Institute of Physics, May 10, 1987, Journal Of Applied Physics, Vol. 61, pp. 4723-4729.

11. **PSIA.** PSIA Park's New AFM Company. *PSIA Website.* [Online] http://psiainc.com/_new/menu031.asp.

12. **W.Cross, John.** Scanning Probe Microscopy. *Scanning Probe Microscopy(SPM)-Imaging Surfaces on a Fine Scale.* [Online] June 13, 2003. [Cited: December 23, 2006.] http://www.mobot.org/jwcross/spm/.

13. **B.Bhushan, H.Fuchs, S.Hosaka.** *Applied Scanning Probe Methods.* Verlag Berlin Heidelberg : Springer, 2004. 1434-4904.

14. **PhotoMetrics, Inc.** Atomic Force Microscope/Scanning Probe Microscopy. *Photometrics.* [Online]

15. **Paul West, Natalia Starostina.** A Guide to AFM Image Artifacts. *Pacific Nanotechnology Website.* [Online] http://www.pacificnano.com/files/pdf_15_1076152090_0.pdf.

16. *Effect of tipmorphology on AFMimages.* **S.H. Ke, T.Uda, I. Stich, K. Terakura.** March 2001, Applied Physics A: Materials Science and Processing, Vol. 72(suppl), pp. S63-S66.

17. *Atomic force microscope tip deconvolution using calibration arrays.* **Goha, Peter Markiewicz and M. Cynthia.** 5, s.l. : American institute of physics, May 1995, Review of Scientific Instruments, Vol. 66, pp. 3186-3190.

18. *An algorithm for surface reconstruction in scanning tunneling microscopy.* **Chicon R, Ortuno M and Abellan.** 1987, Surface Science, Vol. 181, pp. 107-111.

19. *Picture processing and three-dimensional visualization of data from scanning tunneling and atomic force microscopy.* **E.P.Stoll.** 1/2, January 1991, IBM Journal of Research and Development, Vol. 35, pp. 67-77.

20. *A computational model of image process in Scanning X Microscopy.* **H. Gallarda, R. jain.** San Jose : SPIE Symposium on Microlithography, 1991, Proceedings of COnference on Integrated Circuit Metrology, Inspection and Process Control V.

21. *Restoration of Scanning probe microscope images.* **Gopal Sarma Pingali, Ramesh Jain.** Ann Arbor : IEEE, 1992. Proceedings IEEE Workshop on Applications of Computer Vision. p. 282.

22. *Morphological Restoration of Atomic Force Microscopy Images.* **David L Wilson, Kenneth S. Kump, Steven J. Eppell,Roger E. Marchant.** 1, Cleveland : American Chemical Society, October 1994, Langmuir, Vol. 11, pp. 265-272.

23. *Nonlinear digital filtering of scanning-probe-microscopy images by morphological pseudoconvolutions.* **Andrew D. Weisman, Edward R. Dougherty,Howard A. Mizes,FL J. Dwayne Miller.** 4, February 1992, Journal of Applied Physics, Vol. 71, pp. 1565-1578.

24. *Tip characterization and surface reconstruction of complex structures with critical dimension atomic force microscopy.* **G. Dahlen, M. Osborn, N. Okulan, W. Foreman,J. Foucher and A. Chand.** 6, s.l. : American Vacuum Society, December 2005, Journal of Vacuum Science and Technology, Vol. 23, pp. 2297-2303.

25. *Increasing the value of atomic force microscopy process metrology using a high-accuracy scanner, tip characterization, and morphological image analysis.* **J. Schneir, J. S. Villarrubia, T. H. McWaid, V. W. Tsai, and R. Dixson.** 2, April 1996, Journal of Vacuum Science and Technology B, Vol. 14, pp. 1540-1546.

26. *Blind reconstruction of scanning probe image data.* **P. M. Williams, K. M. Shakesheff, M. C. Davies, D. E. Jackson, C. J. Roberts,and S. J. B. Tendler.** 2, s.l. : American Vacuum Society, April 1996, Journal of Vacuum Science and Technology B, Vol. 14, pp. 1557-1562.

27. *Morphological estimation of tip geometry for scanned probe microscopy.* **J.S.Villarubia.** Gaithersburg : s.n., 1994, Surface Science, Vol. 321, pp. 287-300.

28. *Noise-compliant tip-shape derivation.* **P.M. Williams, M.C. Davies, C.J. Roberts, S.J.B. Tendler.** 1998, Applied Physics A: Material science and Processing, Vol. 66, pp. S911-S914.

29. *Application of Neural Networks to the reconstruction of scanning probe microscope imagesdistorted by finite tip sizes.* . **Whitehouse, W L Wang and D J.** 6, s.l. : IOP Publishing Ltd, 1995, Nanotechnology, pp. 45-51.

30. **Palazoglu, Pieter Stroeve and Ahmet.** *Analysis of Atomic Force Micropscopy Images using Wavelet Transforms.* Department of Chemical Engineering and Materials Science, UCDAVIS. Davis : s.n., 2004.

31. **Seeger, Adam.** *Surface Reconstruction From AFM and SEM Images.* Department of Computer Science., University of North Carolina. Chapel Hill : s.n., 2004. PhD dissertation.

32. *Reconstruction of STM and AFM images distorted by finite-size tips.* **Keller, David.** Alburquerque : Surface Science, 1991, Vol. 253, p. 353.

33. *AFM: a versatile tool in biophysics.* **Paolo Facci, Andrea Alessandrini.** s.l. : INSTITUTE OF PHYSICS PUBLISHING, 2005, MEASUREMENT SCIENCE AND TECHNOLOGY.

34. **Fong, Hao.** RESEARCH INTERESTS. [Online] South Dakota School of Mines and Technology, 2003. http://webpages.sdsmt.edu/~hfong/research_interst.html.

35. **Ayres, Virginia.** Research. *Dr. Virginia Ayres, The Electronic and Biological Nanostructures Laboratory.* [Online] 2006. http://virginiaayres.com/research.asp#nb.

36. *A curve fitting procedure and its error analysis.* **I, Kasa.** 1976, IEEE Trans. Inst. Meas., Vol. 25, pp. 8-14.

37. *Scanning Probe Recognition Microscopy Investigation of Tissue Scaffold Properties.* **Y. Fan, Q. Chen, V.M. Ayres, A.D. Baczewski, L. Udpa, and S. Kumar.** East Lansing : s.n., 2006.

38. **Rafael Gonazalez, Richard E. Woods.** *Digital Image Processing.* s.l. : Pearson education, 2002. 8178086298.

39. Atomic Force Microscopy - Tutorial Page. *Pacific Nanotechnology Web Site.* [Online] http://www.pacificnanotech.com/afm-tutorial.html.

40. *Scanning tunneling microscope calibration adn reconstruction of real; elimination, drift and slope elimination.* **Klimov, V. Yu. Yurov and A. N.** 5, s.l. : American Institute of Physics, May 1994, Review of Scientific Instruments, Vol. 65.

41. *Blind restoration method of scanning tunneling and atomic force microscopy images.* **Samuel Dongmo, Michel Troyon,Philippe Vautrot,Etienne Delain,Noe l Bonnet.** 2, s.l. : American Vacuum Society, April 1996, Journal of Vacuum Science and Technology B, Vol. 14, pp. 1552-1556.

42. *Deconvolution of Magnetic Force Images by Fourier Analysis.* **Thomas Chang, Mark Lagerquist, Jian-Gang Zhu,P. B. Fischer,S. Y. Chou and Jack H. Judy.** 5, September 1992, EEE TRANSACTIONS ON MAGNETICS, Vol. 28, pp. 3138-3140.

43. *THREE-DIMENSIONAL PROBE AND SURFACE RECONSTRUCTION FOR ATOMIC FORCE MICROSCOPY USING A DECONVOLUTION ALGORITHM.* **A.A. Bukharaev, N.V. Berdunov, D.V. Ovchinnikov and K.M. Salikhov.** 1, illinois : s.n., 1998, Scanning Microscopy, Vol. 12, pp. 225-234.

44. *Scanned probe microscope tip characterization without calibrated tip characterizers.* **Villarrubia, J. S.** 2, April 1996, Journal of Vacuum Science and Technology B, Vol. 14, pp. 1518-1521.

45. *Scanning Tunneling Microscopy on Rough Surfaces : Deconvolution of COnstant Current Images.* **G. Reiss, f. Schneider, J. vancea, H. Hoffman.** 9, s.l. : American Institute of Physics, August 1990, Applied Physics Letter, Vol. 57, pp. 867-869.

46. *A Novel Algorithm for the Restoration of AFM/STM images.* **Taan-Hu Yu, Sanjit K. Mitra.** April 1994, International Symposium on Speech, Image Processing and Neural Networks, pp. 784-787.

47. **STEFAN THALHAMMER, WOLFGANG M. HECKL.** *Atomic Force Microscopy as a tool in nanobiology Part I: imaging and manipulation in cytogenetics.* s.l. : CANCER GENOMICS & PROTEOMICS 1, 2004.